Geophysical Journal International

Geophys. J. Int. (2017) **209,** 1369–1388
Advance Access publication 2017 March 7
GJI Seismology

doi: 10.1093/gji/ggx096

Internal structure of the San Jacinto fault zone at Jackass Flat from data recorded by a dense linear array

H. Qiu,[1] Y. Ben-Zion,[1] Z.E. Ross,[2] P.-E. Share[1] and F.L. Vernon[3]

[1] *Department of Earth Sciences, University of Southern California, Los Angeles, CA* 90089-0740*, USA. E-mail: hongruiq@usc.edu*
[2] *Seismological Laboratory, California Institute of Technology, Pasadena, CA* 91125*, USA*
[3] *Scripps Institute of Oceanography, University of California San Diego, La Jolla, CA* 92093*, USA*

Accepted 2017 March 6. Received 2017 March 2; in original form 2016 December 5

SUMMARY

The internal structure of the Clark fault in the trifurcation area of the San Jacinto fault zone is imaged using seismograms recorded by a dense linear array (Jackass Flat, JF) crossing the surface trace of the fault and an adjacent array (TR) to the SW. Delay times between phase arrivals associated with ∼3500 local earthquakes and nine teleseismic events are used to estimate velocity variations within the arrays. The teleseismic *P* waves travel faster beneath the TR than the JF array, in contrast to larger scale tomographic results. Statistical analysis of local *P*-wave delay times indicates that the entire JF array, with an aperture of ∼400 m, is inside a low-velocity damage zone. This low-velocity zone is bounded on the NE side by a shallow bimaterial interface generating fault zone head waves, and it contains an inner zone of more intense damage generating fault zone trapped waves. The *P*-wave velocity contrast across the local bounding bimaterial interface is 10–15 per cent. The trapping structure is associated with a width of ∼200 m, *S*-wave velocity reduction of ∼35 per cent with respect to the surrounding rock, *Q*-value of ∼20 and depth of ∼3.5 km. The imaging results suggest that the main seismogenic fault is near the SW end of the JF array, in agreement with a prominent geomorphologic feature. The existence of intense local damage on the crustal block with faster larger scale velocity at depth is consistent with common propagation of earthquake ruptures in the area to the NW.

Key words: Body waves; Earthquake dynamics; Guided waves; Interface waves; Rheology and friction of fault zones; Continental tectonics: strike-slip and transform.

1 INTRODUCTION

Fault zone structures contain important information on various aspects of earthquake and fault mechanics ranging from long-term evolutionary processes to brittle rock rheology and dynamic stress fields operating during the occurrence of earthquakes (e.g. Ben-Zion & Sammis 2003; Xu *et al*. 2012; Rowe & Griffith 2015). Some elements in the core structure of fault zones can control (and reflect past) properties of earthquake ruptures. Specifically, bimaterial interfaces separating different crustal blocks can influence significantly the location, mode, speed and propagation direction of earthquake ruptures (e.g. Weertman 1980; Ben-Zion & Andrews 1998; Brietzke & Ben-Zion 2006; Ampuero & Ben-Zion 2008; Brietzke *et al*. 2009; Shlomai & Fineberg 2016), and hence generated ground motion (e.g. Olsen *et al*. 2006; Kurzon *et al*. 2014). A low-velocity fault zone layer can produce oscillations of rupture velocity and slip rate (e.g. Ben-Zion & Huang 2002; Huang *et al*. 2014) and promote rupture propagation (Weng *et al*. 2016). Asymmetric rock damage across the seismogenic fault may indicate repeating occurrence of large earthquake ruptures with statistically preferred propagation direction (e.g. Ben-Zion & Shi 2005; Lewis *et al*. 2005; Dor *et al*. 2006, 2008).

The surface expressions of fault zones often have high geometrical complexity with hierarchical damage zones and multiple surface traces. This surface complexity and the diffuse character of low magnitude seismicity (Fig. 1) make it difficult to identify the main seismogenic fault. In this paper, we attempt to clarify the location at seismogenic depth and internal structure of the Clark fault in the trifurcation area of the San Jacinto fault zone (SJFZ), about 30 km southeast of Anza, California. The SJFZ is the most seismically active fault zone in southern California (Hauksson *et al*. 2012) and accommodates a large portion of the plate motion in the region (e.g. Fay & Humphreys 2005; Lindsey & Fialko 2013). Palaeoseismic and historic records indicate that the SJFZ is capable of large ($M_w > 7.0$) earthquakes (e.g. Petersen & Wesnousky 1994; Onderdonk *et al*. 2013; Rockwell *et al*. 2015) that pose significant seismic hazard to large urban areas in southern California.

Allam & Ben-Zion (2012), Allam *et al*. (2014a) and Zigone *et al*. (2015) derived earthquake- and noise-based tomographic models for the region around the SJFZ. These studies imaged with nominal

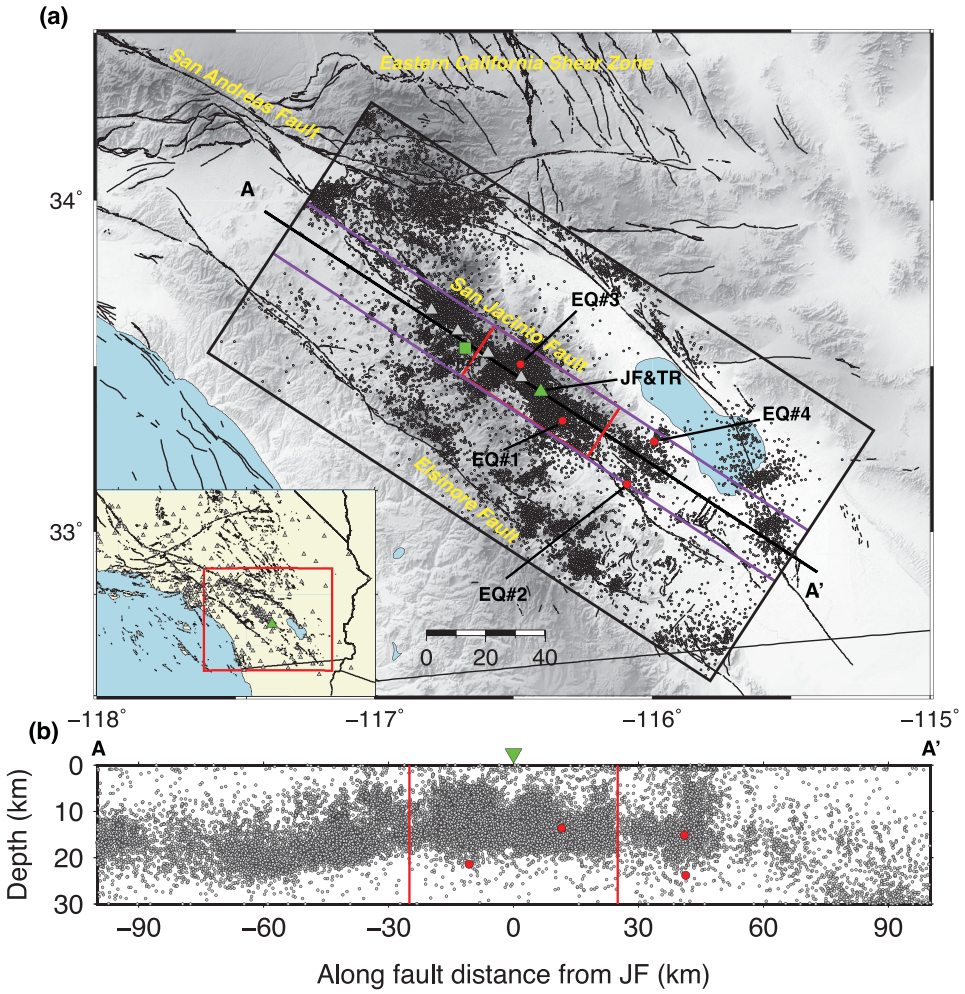

Figure 1. (a) Location map for the San Jacinto fault zone (SJFZ) with 28 995 earthquakes used in this study (circles). The green triangle marks the location of JF and TR fault zone arrays that are the focus of this paper. Other fault zone arrays are marked by grey triangles. The town of Anza and surface traces of faults are shown by a green square and black lines, respectively. Events analysed for fault zone trapped waves (FZTW), fault zone head waves (FZHW) and *P* delay times are contained within the black, purple and red boxes, respectively. Data from the events marked by red circles are illustrated in later figures. (b) Depth section of hypocentres projected along the cross-session AA′ in (a). The locations are poorly constrained for along-fault distances larger than ∼50 km because of reduced network converge.

resolution of 1–2 km several key structural features including overall velocity contrasts across the SJFZ and damage zones at different locations. Here, we image internal components of the Clark fault in the trifurcation area with spatial resolution ranging from a few 100 m wide damage zones down to a local bimaterial interface. The imaging employs earthquake data recorded by a dense linear array crossing the Clark fault at the Jackass Flat (JF) site, and a sparser adjacent array (TR). These arrays are part of a PASSCAL deployment starting in 2010 of five linear arrays crossing the SJFZ at different locations (triangles in Fig. 1) and additional near-fault sensors (Vernon & Ben-Zion 2010). The JF array crosses the surface trace of the Clark fault in relatively flat topography and it has nine broad-band seismometers with ∼20–30 m spacing between instruments in the centre and a total aperture of ∼400 m. The TR array southwest of the JF array is situated about 100 m higher with four broad-band seismometers having ∼0.5–1 km station spacing, and it does not cross the surface trace of any large fault (Fig. 2).

The tomographic results for the area indicate a large-scale lithology contrast across the seismogenic fault at JF, with slower and faster *P*-wave velocities on the SW and NE sides, respectively (Fig. 3). The TR array is on the slower SW side of the fault, while the JF array appears to cross the boundary between the two blocks although this is not clear given the 1–2 km resolution of the velocity model. In the following sections, we provide detailed results on the velocity structure below the JF and TR arrays using local and teleseismic earthquake data and several types of analyses. In Section 2, we describe the data used in this study. Section 3 presents results based on delay times of *P* waves at stations across the arrays, and analyses of fault zone head and trapped waves recorded by the JF array. The results indicate that the main seismogenic fault is close to the SW end of the JF array, and the existence of a significant shallow local low-velocity zone (LVZ) NE of the fault. The latter produces a local reversal to the overall large-scale velocity contrast consistent with persistent preferred propagation direction of earthquake ruptures to the NW.

2 DATA

The data analysed in this work consist of waveforms of ∼29 000 local and nine teleseismic earthquakes recorded during 2012–2014

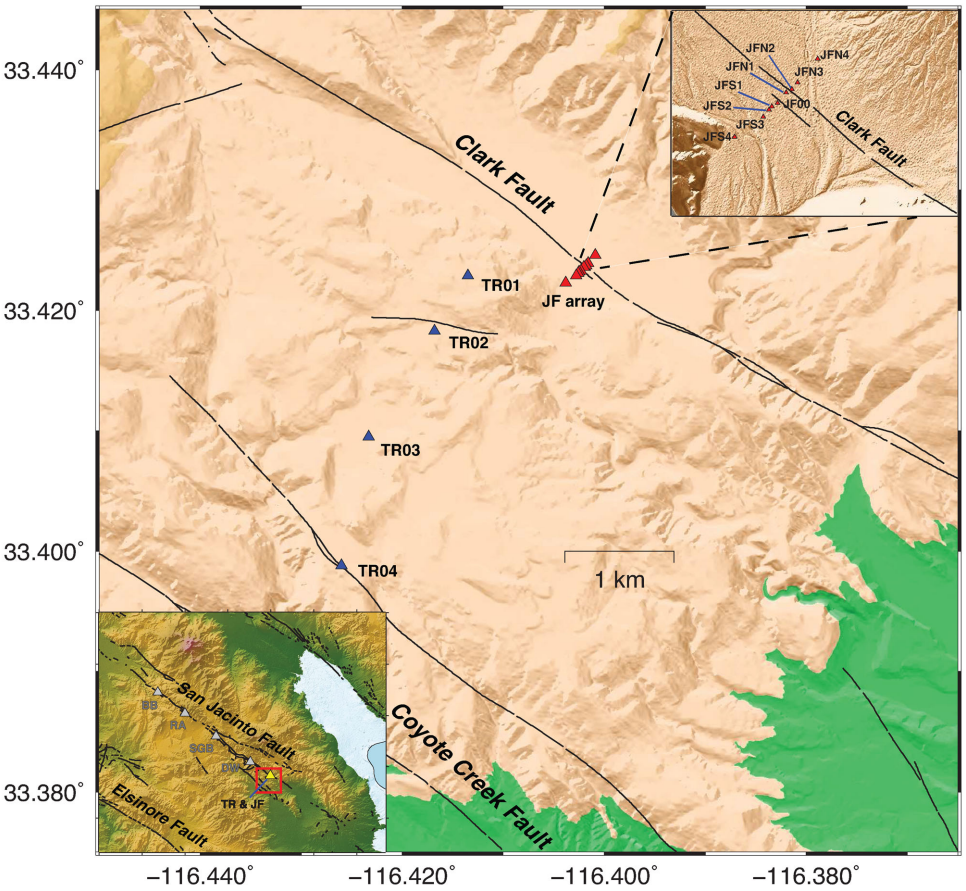

Figure 2. Location map for the JF and TR arrays at the SE end of the Clark fault. The JF array has nine stations separated by ∼20–30 m in the centre with a total aperture of ∼400 m, and is located on relatively flat topography (top right inset). The TR array to the SW has four stations separated by 0.5–1 km, with elevation ∼100 m higher than the JF array.

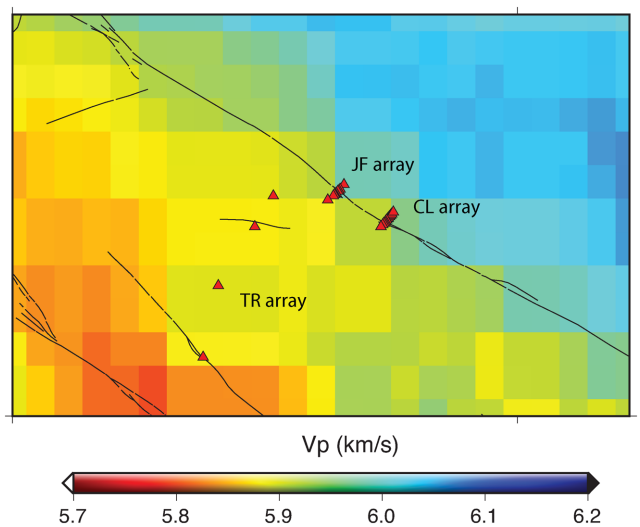

Figure 3. Average *P*-wave velocity over the depth range 1–7 km based on tomographic results of Allam & Ben-Zion (2012). Red triangles indicate stations of the JF and TR arrays, as well as a nearby CL array deployed in 1999.

with 200 Hz sampling rate by the JF and TR arrays located in the JF area (Fig. 2). The local earthquakes are taken from a catalogue for the SJFZ region utilizing the Anza network and nearby stations of the regional southern California network and several local deployments (White *et al*. 2016). The corresponding waveforms are extracted from the YN data set available at the IRIS Data Management Center (Vernon & Ben-Zion 2010). The black and purple rectangles in the top panel of Fig. 1 show events used for analysis of fault zone trapped and head waves, respectively, while the red rectangle indicates events used for slowness analysis. Arrival times of *P* and *S* body waves generated by the local events are found with the automated phase picking algorithms of Ross & Ben-Zion (2014) and Ross *et al*. (2016). Initial detection of candidate fault zone head and trapped waves are made with the automated algorithms of Ross & Ben-Zion (2014, 2015). The nine analysed teleseismic events and corresponding waveforms are taken from the SCSN catalogue and Southern California Earthquake Data Center (SCEDC 2013). These events have $M > 6$ and depth > 60 km. They are selected for analysis because their recorded waveforms have sufficient signal-to-noise ratio (SNR) in a frequency band 0.01–0.5 Hz used in our analysis. The traveltime of the teleseismic phases at the JF and TR arrays are predicted using the global 1-D velocity model IASP91 (Kennett & Engdahl 1991). The waveforms, arrival times and detected fault zone waves are analysed in detail below.

3 ANALYSIS

Four types of studies involving different signals and scales are conducted to image the internal structure of the SJFZ at the JF area: teleseismic delay time analysis (DTA), local *P*-wave DTA and

analyses associated with fault zone head waves (FZHW) and fault zone trapped waves (FZTW). The analyses are described below starting with large-scale structural features and progressing to inner fault zone components.

3.1 Teleseismic arrival time delay analysis

3.1.1 Methodology

The selected teleseismic waves sample the crustal structure with near-vertical incidence angles at lower frequencies than the local seismic waves. The relative arrival time delays of teleseismic phases across an array can be used to infer variations in crustal velocity structure below the stations (e.g. Cochran *et al*. 2009). If the array across a fault has large enough aperture, the delays can further be used to quantify the average velocities of the different crustal blocks separated by the fault (Ozakin *et al*. 2012). The JF and TR arrays have small apertures and are located (Fig. 3) within a broad low-velocity damage zone that extends over the top 5 km or so of the crust (Allam & Ben-Zion 2012; Allam *et al*. 2014a; Zigone *et al*. 2015). This configuration is not suitable for imaging with teleseismic arrivals the deep structure across the fault, but can be used to image variations within the damage zone and clarify the location of the seismogenic fault.

We examine delay times of teleseismic *P* and *pP* phases across the stations, focusing on frequency ranges with significant recorded spectral energy. For a low-frequency band, where the structure is being sensed more broadly by the teleseismic waves, the delay times between different stations are suitable for analysing larger scale velocity variations and can be applied to an array with large station spacing. In the high-frequency case, the delay times are more sensitive to the local velocity variations, and can only be derived robustly with small station separations. As the frequency content of a teleseismic phase varies between events, we study the teleseismic delay time separately for each individual teleseismic earthquake.

Figs 4 and 5 illustrate the analysis of teleseismic *P* and *pP* phases generated by a deep event with $M = 6.5$ (additional details are

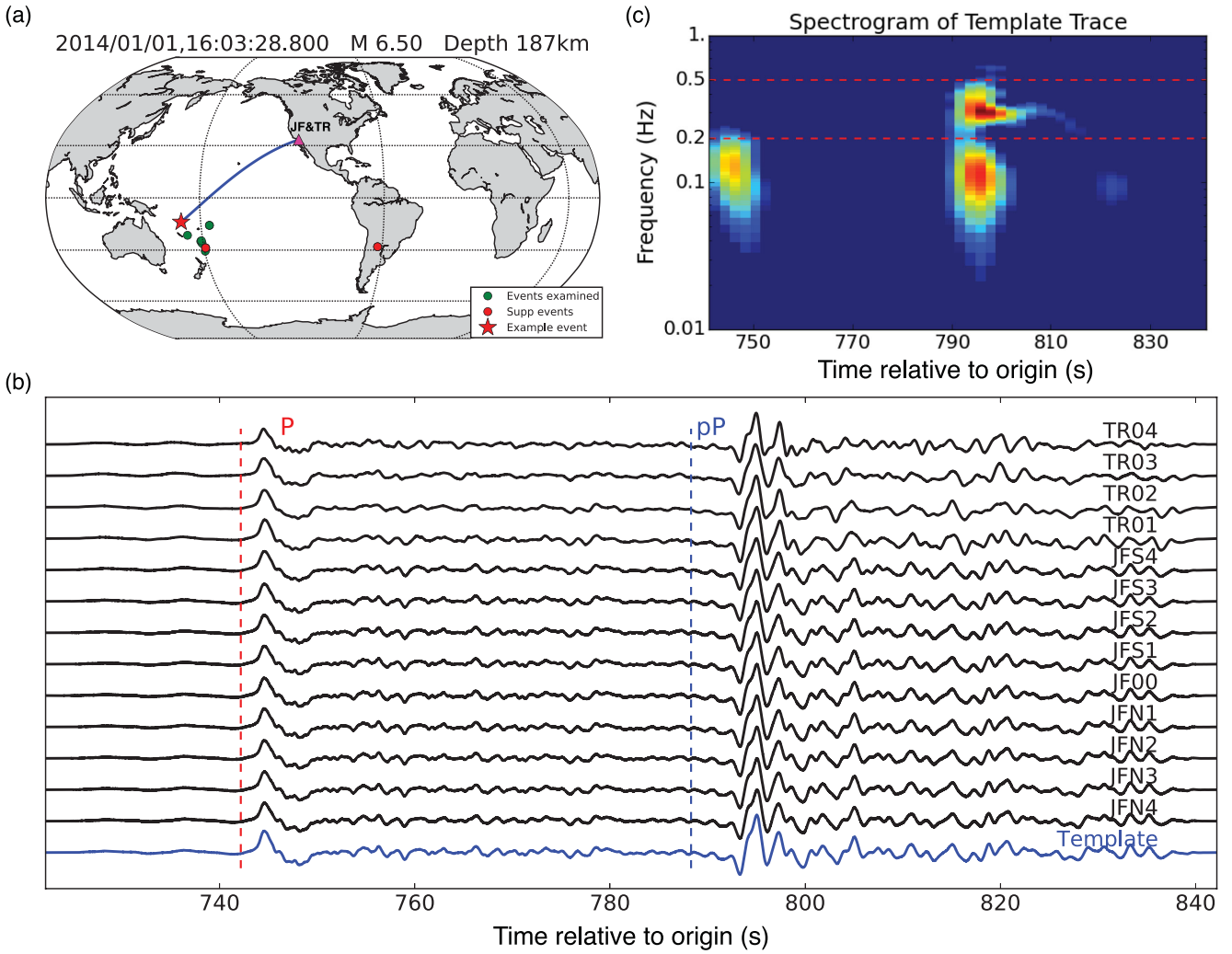

Figure 4. Teleseismic data recorded at the JF and TR arrays. (a) Red star and circles denote locations of events analysed in the main text and Supporting Information, respectively, while green circles indicate additionally examined events. (b) Velocity seismograms at the JF and TR arrays with the *P* and *pP* phases generated by the event denoted by the red star in (a), and template produced by averaging the seismograms recorded by the JF array (bottom trace). The red and blue dashed lines mark predicted arrival times based on the IASP91 global velocity model. (c) Spectrogram of the template trace with amplitudes ≥35 per cent of the maximum value (colours). The *P* phase energy is mostly below 0.2 Hz, while the *pP* phase has one-energy amplitude below 0.2 Hz and another between 0.2 and 0.5 Hz.

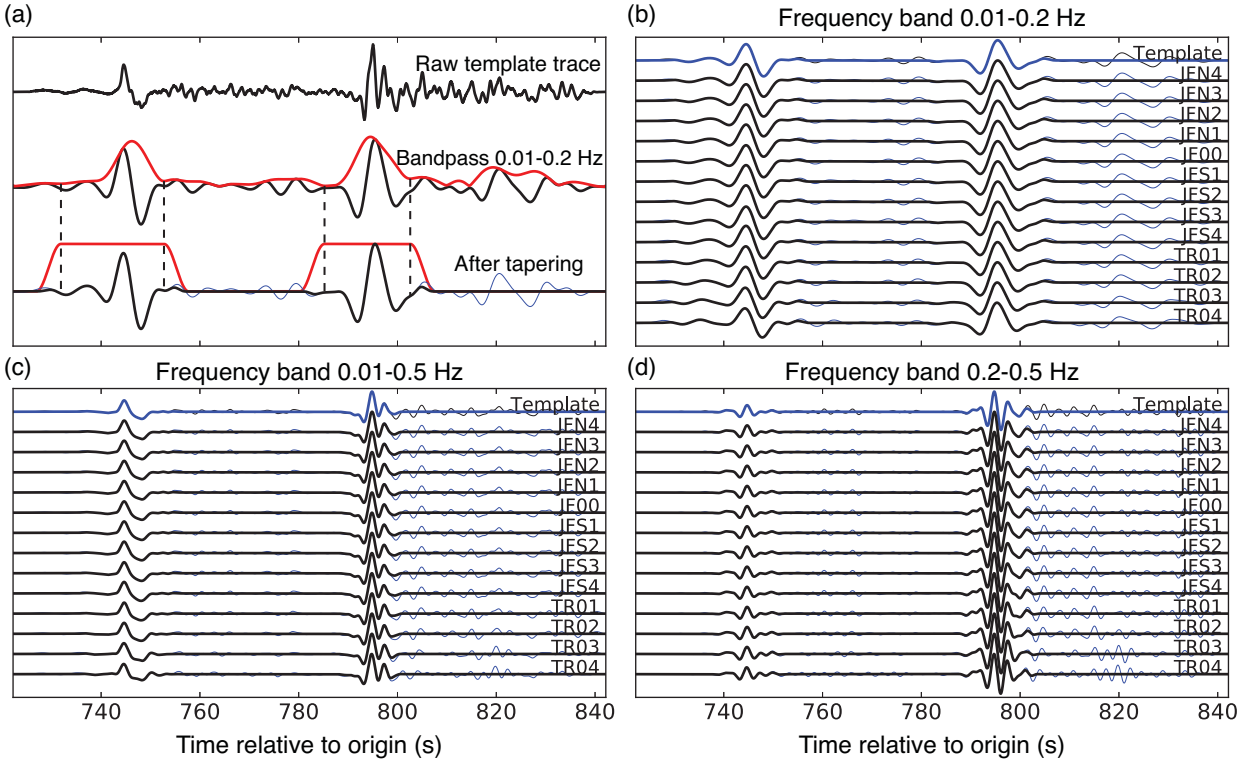

Figure 5. (a) Tapering window construction for teleseismic *P* and *pP* phases at 0.01–0.2 Hz. Raw template trace on top is first bandpass filtered at the target frequency range (middle black seismogram). Then, an envelope function is computed (red curve in the middle) and a tapering window is built using the two nearest local minima (dashed lines) around the peak amplitudes corresponding to the *P* and *pP* phases. The template traces before (purple) and after (black) tapering are shown in the bottom. (b) Comparisons between velocity seismograms of teleseismic *P* and *pP* phases before and after tapering. (c) Same as (b) for 0.01–0.5 Hz. (d) Same as (b) for 0.2–0.5 Hz.

given in the next subsection). Since the station spacing within the JF array is much smaller than the TR array, we generate a template trace by stacking all waveforms observed at the JF array (Fig. 4b, bottom trace). Examining the dominant frequency bands in the spectrogram of the template trace (Fig. 4c) indicates two frequency bands (0.01–0.2 and 0.2–0.5 Hz) with sufficient energy. Next, we filter the waveforms at each frequency band and produce shorter waveforms around each teleseismic phase. We select tapering windows around the phases using two steps. First we filter the template trace to the target frequency range (e.g. 0.01–0.2 Hz in Fig. 5a) and compute a corresponding envelope function (middle red curve in Fig. 5a). Then, we locate the peak amplitude, $t_{\rm peak}$, of the *P* or *pP* phase in the envelope function, find the nearest local minimums, $t_{\rm min1}$, $t_{\rm min2}$, in the envelope function before and after the peak, and construct a tapering window such that the signal between $t_{\rm min1}$ and $t_{\rm min2}$ remains unchanged (bottom red curve in Fig. 5a).

For the *i*th station, the time-shift $\tilde{T}_i$ of a given phase is derived by cross-correlating the truncated waveform around the target phase with that of the template trace. To obtain delay time $T_{\rm i}$ associated with the local velocity structure, we have to correct for expected delays due to topography and the geometry of the stations and incoming plane wave. This is done by applying the following two-step corrections on $\tilde{T}_i$.

(1) For station *i*, the traveltime of a target teleseismic phase is estimated with the TauP toolkit (Crotwell *et al*. 1999) assuming the IASP91 global velocity model and that the station is at sea level. The expected traveltime delay at the *i*th station due to the geometry of the stations and incoming plane wave is approximately given by

$$\Delta\tilde{t}_i = \tilde{t}_i - \left[\sum_{i=1}^{n} \tilde{t}_i\right]/n, \tag{1}$$

where *n* is the number of stations considered in the analysis.

(2) Assuming the teleseismic phase is traveling with vertical incident angle in the top portion of the crust, the relative altitude at station *i* can be written as $\Delta h_i = h_i - [\sum_{i=1}^{n} h_i]/n$ with $h_{\rm i}$ being the station elevation. The delay in arrival time caused by topography is given by $\Delta\tilde{\tau}_i = \Delta h_i/v_{\rm ref}$, where $v_{\rm ref}$ is the velocity of the target phase in the top crust. The delay time at station *i* can then be estimated as

$$T_i \approx \tilde{T}_i - \Delta\tilde{t}_i - \Delta\tilde{\tau}_i. \tag{2}$$

The spatial pattern of the delay time $T_{\rm i}$ across the fault zone arrays can be derived for different frequency ranges using the described steps. Fig. 6 shows schematically expected delay time patterns associated with two ideal conceptual fault models. By comparing the obtained teleseismic delay times with the schematic patterns, we can estimate the basic type of crustal structure beneath the arrays.

3.1.2 Results

Continuing with the example teleseismic event of Fig. 4, the spectrogram for the *P* wave exhibits a clear dominant frequency of ∼0.15 Hz and the *pP* phase has two clear energy peaks, one below 0.15 Hz and another between 0.2 and 0.5 Hz (Fig. 4c). We there-

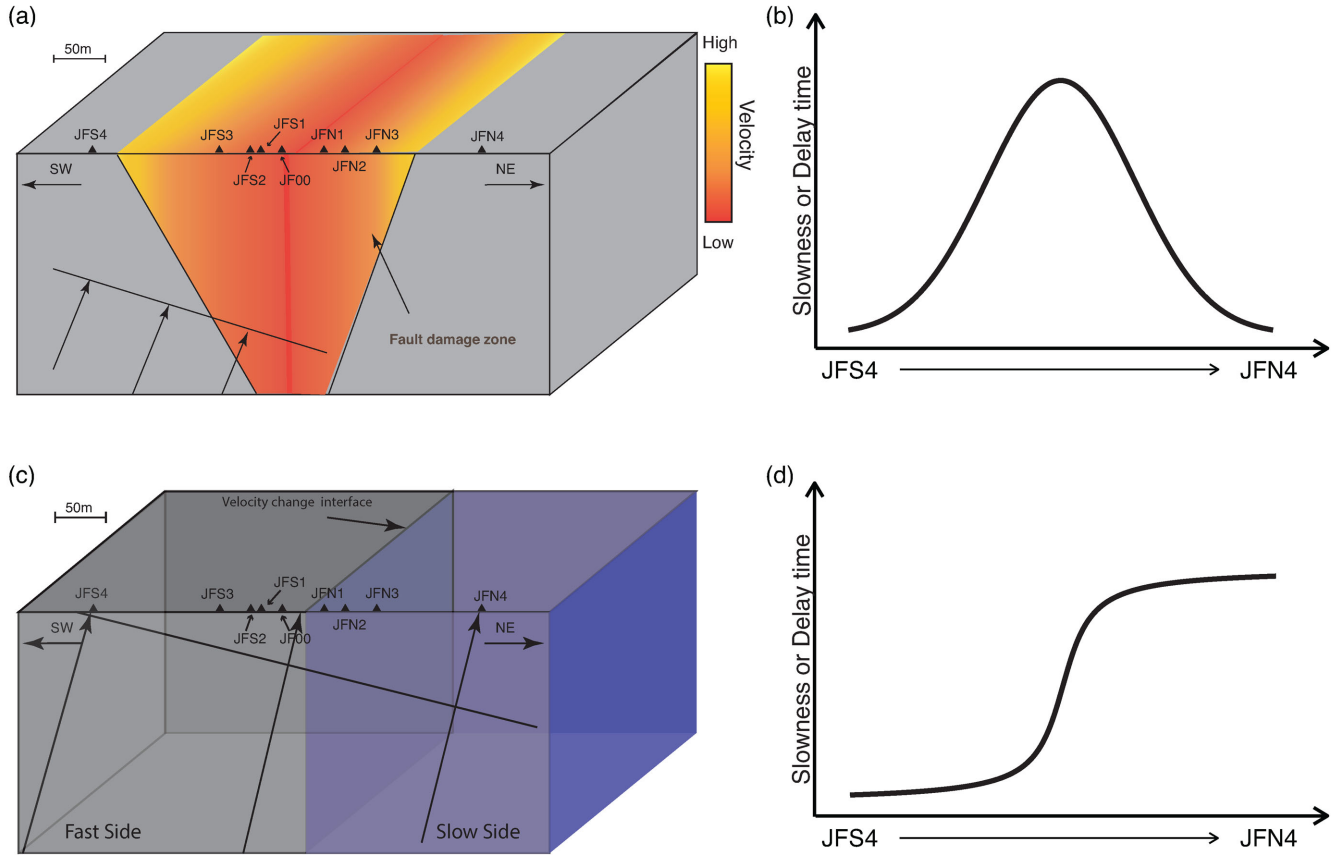

Figure 6. Schematic diagrams of slowness patterns for two different fault models. (a) A model with a fault damage zone beneath the array. (b) Slowness pattern expected for the model in (a). (c) A structure with a velocity contrast across the fault. (d) Slowness pattern expected for the model in (c).

fore compute delay time patterns for this event using the overall frequency band 0.01–0.5 Hz and two subranges 0.01–0.2 Hz and 0.2–0.5 Hz. Figs 5(b)–(d) present waveforms bandpass filtered in these frequency ranges. Although the spectrogram in Fig. 4(c) does not show strong signal above 0.2 Hz for the *P* phase, the teleseismic *P* phase appears clearly in the waveforms after bandpass filtering at 0.2–0.5 Hz (Fig. 5d). As mentioned, we taper the waveform around a given target teleseismic phase before calculating cross-correlations for time delays. Comparisons of results with different tapering choices indicate that the *P* waveforms are less sensitive than the *pP* waveforms to details of the tapering for all three frequency bands. We therefore analyse only delay time patterns associated with the *P* phases.

Figs 7(a)–(c) show delay times for teleseismic *P* waves associated with the three used frequency bands. Since the station spacing in TR array (∼1 km) is much larger than the JF array (∼20 m), we only calculate the delay times for TR array at 0.01–0.5 Hz. The delay times are only 3–4 sampling intervals, but the patterns show persistent variations of progressive velocity reduction from the SW to the NE (TR04 to JF00). The overall delay time pattern across the arrays remains when the reference velocity used for correcting the topography of the TR array varies in the range 2–6 km s^{-1} (different lines in Fig. 7a). The same holds for corresponding results associated with other examined teleseismic events. The detailed variations across the JF array associated with the overall frequency range 0.01–0.5 Hz (Fig. 7a, right) are consistent with the schematic pattern in Fig. 6(d), suggesting a possible vertical velocity interface separating two crustal blocks between stations JFS3 and JFN1. The delay time patterns calculated for the JF array at frequency ranges 0.01–0.2 and 0.2–0.5 Hz are displayed (Figs 7b and c) in the same range outlined by the red dashed box in Fig. 7(a). The results computed at the lower frequency 0.01–0.2 Hz are similar to those at the overall range 0.01–0.5 Hz. However, for the higher frequency range 0.2–0.5 Hz, the delay time reaches a maximum at stations JFN1 and JFN2, still with generally more delay in the NW (JF00–JFN4) than the SW side (JFS4–JFS1). This pattern is similar to the schematic curve in Fig. 6(b), suggesting a LVZ beneath the centre of the array. These inferences are supported by results based on additional teleseismic events, two of which shown in Figs S1 and S2 in the Supporting Information, and slowness analysis using ∼3500 local events enclosed in the red box of Fig. 1 (Section 3.2).

To summarize, *P* waves travel faster beneath the TR than the JF array at the overall frequency range of 0.01–0.5 Hz, in contrast with the expectation from the larger scale tomography results of lower seismic velocities to the SW of the SJFZ (Fig. 3). The delay times calculated within the JF array imply the existence of both an LVZ underneath the centre of the array and a potential vertical velocity interface possibly located between stations JFS3–JFN1. The reversed local shallow velocity contrast across the fault compared with the large-scale seismogenic contrast is consistent with observations presented in later sections, observed trapping structure to the NE of the fault at the nearby CL array (Lewis *et al*. 2005) and rock damage asymmetry across the fault based on analysis of geomorphology features (Wechsler *et al*. 2009). The local shallow reversal of the velocity contrast across the fault can be explained by bimaterial ruptures on the SJFZ in the area with preferred propagation direction to the NW (Ben-Zion & Shi 2005; Xu *et al*. 2012).

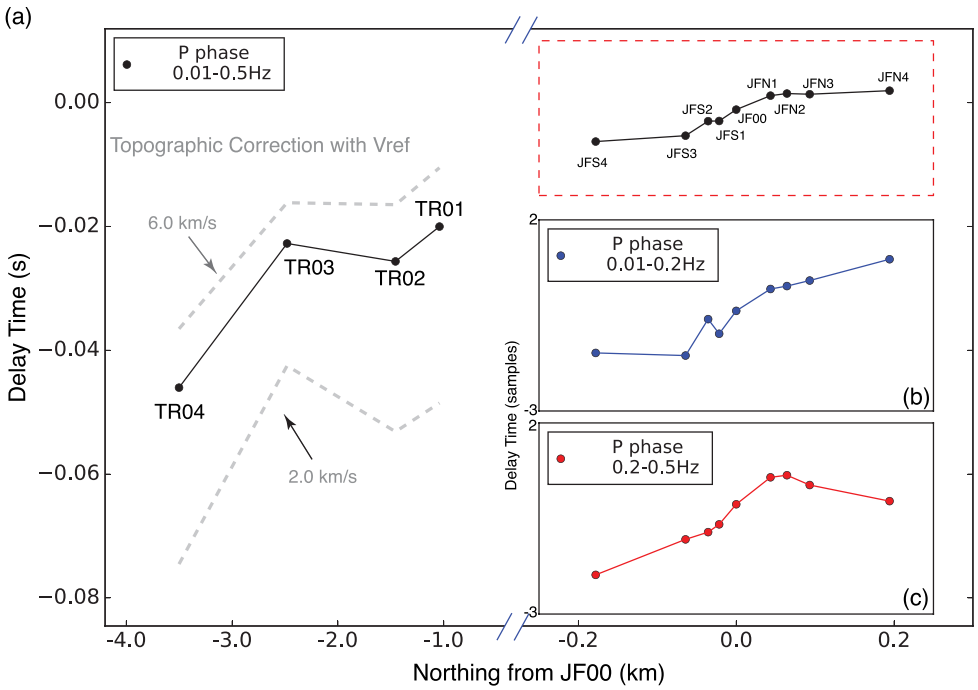

Figure 7. (a) Delay times for teleseismic *P* phase at 0.01–0.5 Hz. The observed variations in *P* arrivals are corrected with the traveltime delays due to the geometry of the station and incoming plane wave and topography. The black dots denote delay times derived using 4 km s^{-1} reference velocity in topographic correction. The grey dashed lines indicate the lower and higher bound of delay times computed at the TR array using reference velocities of 2 and 6 km s^{-1}, respectively. (b) Delay times for teleseismic *P* phase at 0.01–0.2 Hz. The delay times (blue dots) are shown in the same range outlined by the red dashed box in (a) at the JF array. (c) Same as (b) for 0.2–0.5 Hz.

3.2 Local *P*-wave delay time analysis

3.2.1 Methodology

Direct *P*-wave arrival times from local earthquakes recorded at a dense array can provide detailed information on the local fault zone structure. Similar to teleseismic arrivals, the variations in direct *P* arrivals across the array reflect (with higher frequencies sensitive to smaller scale features) the geometrical effect of wave propagation and heterogeneous velocity structure below the array. Given the relatively large spacing between stations of the TR array and high frequencies of the local data, we focus here on data recorded by the JF array only. After removing the geometrical effect of the array geometry, the remaining delay time pattern across the array indicates how *P*-wave arrivals are affected by the local velocity structure. The use of traveltimes from thousands of local earthquakes provides statistically robust estimates of local velocity changes across the array.

We first obtain automatic *P* picks (red triangles in Fig. 8) using the algorithm of Ross & Ben-Zion (2014). Analysis of significant number of local earthquakes in the Parkfield area indicates that the median and standard deviation of the differences between manual and automatic *P* picks are 0.004 and 0.023 s, respectively (Ross & Ben-Zion 2014). These values imply that the errors in automatic *P* picks are negligible for the performed statistical analysis of *P*-wave delay time pattern. Fig. 8 illustrates different arrival patterns at the JF array with data of four example earthquakes. For events EQ#1 and EQ#2 southwest of the fault (Fig. 1), the *P* waves arrive earlier at the southwestern most station JFS4 compared to the northeastern most station JFN4. The trend reverses for events EQ#3 and EQ#4 that are northeast of the fault (Fig. 1). These results indicate a directional dependent arrival pattern due to the source–receiver geometries.

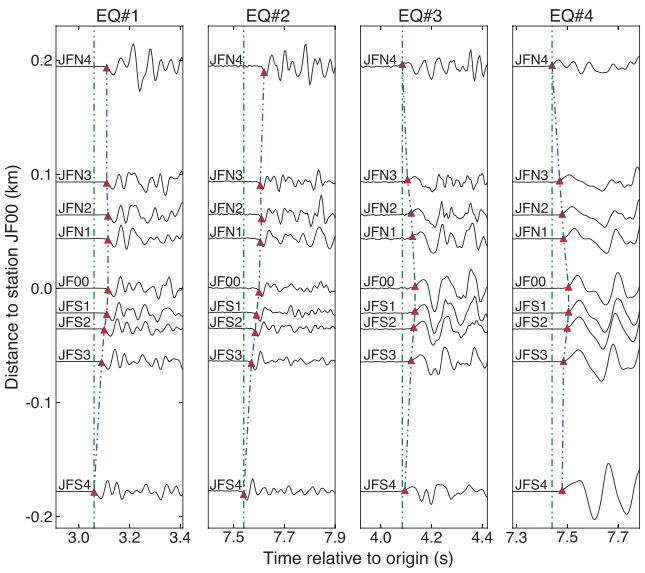

Figure 8. Early *P*-wave velocity seismograms recorded at the JF array for events marked as red circles in Fig. 1. The red triangles denote the automatic *P*-wave picks. The green and blue dashed lines indicate the time of the earliest arriving phase and the interpolated *P*-wave traveltime across the array, respectively.

However, in all four examples, the direct *P* waves arrive later at the central stations JFS1, JF00 and JFN1 (Fig. 8). This consistent late arrival pattern, independent of the earthquake backazimuth, is produced by a local velocity structure beneath the array.

For a linear array with aperture much smaller than the hypocentre distance, the variations in traveltime due to the different receiver

locations can be estimated using a 1-D velocity model. To have a representative 1-D velocity model, we average horizontally the 3-D *P*-wave velocity model of Allam & Ben-Zion (2012) for the SJFZ region. The results remain essentially the same when using a combined velocity model based on the results of Allam & Ben-Zion (2012), Allam *et al*. (2014a) and Zigone *et al*. (2015). The 1-D velocity model is used to compute predicted *P* arrival time $\tilde{t}_{ij}$ based on the algorithm of Kissling (1988) for each *i*–*j* earthquake-station pair. Subtracting the predicted arrival at the central station JF00 gives predicted changes $\Delta\tilde{t}_{ij} = \tilde{t}_{ij} - \tilde{t}_{ij_0}$ of the *P* arrivals from station JF00 due to the different propagation distances within the array. This does not remove completely the geometrical effect, but averaging results for all used earthquakes reduces further this source of variations.

The traveltimes of *P* waves depend on the hypocentral distance. To compare results associated with different source–receiver distances, we compute the average slowness α_{ij} over the entire ray path between sources *i* and receivers *j* in the following way. We first approximate the propagation distance with the theoretical ray length $\tilde{\Delta}_{ij_0}$ from each earthquake to the reference central station JF00 based on the 1-D velocity model. Using the observed *P*-wave traveltime t_{ij}, the average slowness is estimated as

$$\alpha_{ij} = \left(t_{ij} - \Delta\tilde{t}_{ij}\right) \Big/ \tilde{\Delta}_{ij_0}, \tag{3}$$

where $\Delta\tilde{t}_{ij}$ is the delay time correction for the geometrical effect for earthquake *i* at station *j*. The average slowness α_{ij} can still have systematic variations with the source location. For example, the average slowness tends to be larger for shallow earthquakes than deeper ones. To reduce the variability due to source location in the statistical analysis, we define relative slowness as

$$\alpha_{ij}^{R} = \alpha_{ij} / \sum_{j=1}^{n} \alpha_{ij} / n, \tag{4}$$

where *n* is the number of stations used in the analysis. The dimensionless relative slowness α_{ij}^{R} quantifies the relative relationship between the average slowness estimated at each station and the arrays mean slowness value.

3.2.2 *Results*

Fig. 9 shows for the example event EQ#3, the observed *P* arrivals, along with the estimated average and relative slowness for the JF array. To infer the velocity variations underneath the array, we evaluate statistically the patterns of both average slowness and relative slowness associated with many events. To filter erroneous *P* picks and obtain robust *P* delay times, we require the *P*-wave SNR to be larger than 30.0 and *P*-wave apparent velocity along the orientation of the array to be larger than 14.0 km s^{-1}. To ensure the 1-D velocity model used to correct for basic propagation effects is a good approximation for the medium the waves travel through, we also reject *P*-wave traveltimes not within ±1 s from the prediction based on the velocity model.

The local *P*-wave DTA analysis for the JF array starts with ∼7800 earthquakes within 10 km from the fault and within along-strike distance from the JF array of 25 km (red box in Fig. 1). Events not satisfying the above quality criteria are dropped, leaving ∼3500 events for refined statistical analysis of average slowness and relative slowness of *P* wave at stations across the JF array. Figs 10(a) and (b) show histograms of average slowness and relative slowness for station JF00, respectively. As indicated by the range of horizontal axes, the width of average slowness distribution is much larger than

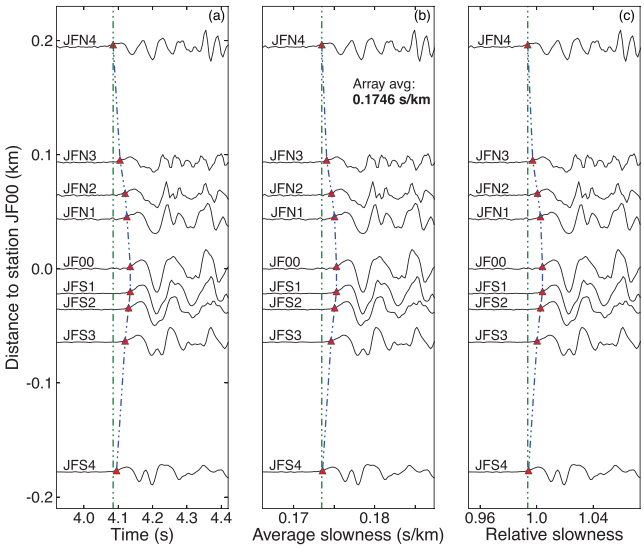

Figure 9. Illustration of the slowness calculation in local *P*-wave data. (a) Early *P*-wave velocity seismograms for event EQ#3 (see Fig. 1 for location) with the red triangles indicating the automatic *P* picks. Each seismogram is shifted in time by the delay due to geometrical effect predicted by a 1-D velocity model. (b) Same as (a) with horizontal axis normalized by the theoretical ray length between the hypocentre and reference station JF00. The red triangles denote the slowness estimates with an average value across the array of 0.1746 km s^{-1}. (c) Same as (b) with horizontal axis normalized by the mean average slowness value across the array calculated in (b). The relative slowness values are given by the red triangles.

that of the relative slowness. Using similar histograms for other stations of the JF array, the mean value and standard deviation of the mean for the average and relative slowness distributions are calculated at each station. Fig. 10(c) summarizes the mean values of the average slowness (green) and relative slowness (black) together with two times their standard deviation as error bars across the JF array. The two curves, scaled to have similar overall amplitudes, collapse on the same pattern with difference primarily in the error bars.

The patterns of the two slowness curves in Fig. 10(c) are similar to the one depicted in Fig. 6(b), with a zone of larger slowness at the central part, possibly indicating a damaged zone at the centre of the array (Fig. 6a). No significant step of the type illustrated in Figs 6(c) and (d) is observed in the local *P*-wave DTA within the JF array. The shape of the slowness patterns in Fig. 10(c), obtained using local *P* arrivals averaged over thousands of events coming from different azimuths, is consistent with the delayed time curve computed for teleseismic *P* phase at 0.2–0.5 Hz (Fig. 7c). The dominant frequency of *P* wave generated by the local earthquake is approximately 10 Hz. The delays of *P* waves generated by local events and those produced by teleseismic events at frequencies above 0.2 Hz are likely dominated by the local shallow low-velocity FZ structure underneath the JF array.

3.3 Fault zone head wave

3.3.1 *Methodology*

FZHW are emergent seismic phases that refract along a bimaterial interface in the fault zone structure, propagating along the interface with the faster wave speed and radiated from there to the slower velocity medium (Ben-Zion 1989, 1990). In a simple model with

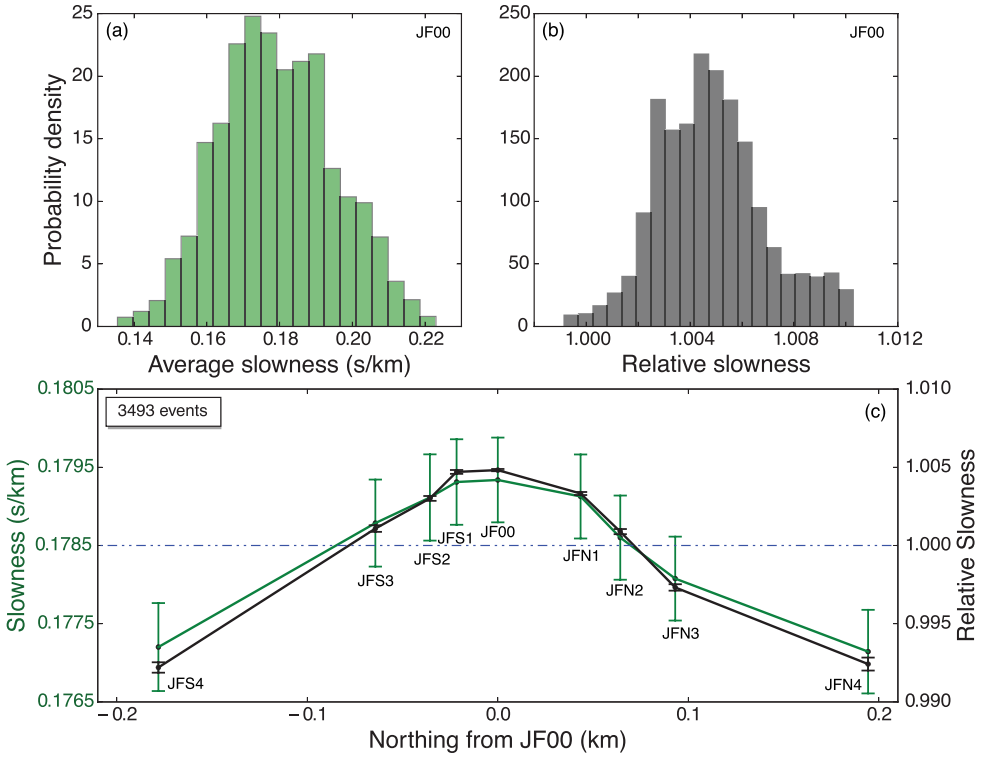

Figure 10. (a) Histogram of average slowness for station JF00. (b) Same as (a) for relative slowness. (c) Mean values of the average slowness (green) and relative slowness (black) computed for 3493 events at the JF array. Error bars indicate a range of two standard deviations about each respective mean value. The horizontal dashed line denotes the mean value of average and relative slowness across the array.

two different quarter spaces in contact, FZHW are the first arrivals at stations on the side with slower seismic velocity having normal distance from the interface x less than a critical distance x_c given by

$$x_c = r \cdot \tan\left(\cos^{-1}\left(\alpha_s/\alpha_f\right)\right), \tag{5}$$

where r is the propagation distance along the bimaterial interface and α_f and α_s are the P-wave velocities of the faster and slower media, respectively. The traveltime of FZHW generated by events on the interface and recorded by stations on the slow side can be expressed (Ben-Zion 1989) as

$$t_H = r/\alpha_f + x\sqrt{\alpha_s{}^{-2} - \alpha_f{}^{-2}}, \tag{6}$$

while the corresponding traveltime of the direct P wave is

$$t_P = \sqrt{r^2 + x^2}\Big/\alpha_s. \tag{7}$$

The moveout between the FZHW and direct P arrival $\Delta t = t_P - t_H$ for a station on the fault is

$$\Delta t = r/\alpha_f \cdot \eta/(1-\eta), \tag{8a}$$

where η is the fractional velocity contrast defined as $(\alpha_f - \alpha_s)/\alpha_f$. In cases when $\eta \ll 1$, the moveout is given approximately by

$$\Delta t \approx r \cdot \Delta\alpha/\alpha^2, \tag{8b}$$

where α and $\Delta\alpha$ denote the average and differential P-wave velocities, respectively (Ben-Zion & Malin 1991). In addition, the moveout Δt decreases monotonically with increasing station distance x from the interface.

Observed FZHW and these relations were used in various studies to image properties of bimaterial fault interfaces at sections of the San Andreas fault in California (e.g. McGuire & Ben-Zion 2005; Zhao *et al*. 2010; Share & Ben-Zion 2016), the North Anatolian fault in Turkey (Bulut *et al*. 2012; Najdahmadi *et al*. 2016) and other faults (e.g. Hough *et al*. 1994; Zhao & Peng 2008; Yang *et al*. 2015). FZHW also have horizontal particle motion (HPM) with a significant fault-normal component, since they are radiated from the fault, in contrast to the particle motion of the direct P wave that points in the epicentre direction (e.g. Bulut *et al*. 2012; Allam *et al*. 2014b).

Ross & Ben-Zion (2014) developed an automatic detector that searches the early P waveform for a possible emergent phase before a sharper arrival, with a time separation between a minimum value (0.065 s representing the width of a narrow P-wave wiggle) and a maximum value (corresponding to a 10 per cent velocity contrast). The method was tested systematically on both synthetic seismograms generated with the solution of Ben-Zion & Aki (1990) and observed data in the Parkfield area where FZHW were detected manually before (Zhao *et al*. 2010). We begin the analysis of FZHW by running the detection algorithm of Ross & Ben-Zion (2014) on waveforms generated by >18 000 earthquakes that are within 10 km from the fault (purple box in Fig. 1). To validate the FZHW detections, we visually inspect how the moveout between tentative FZHW picks and direct P arrivals changes across stations of the JF array. Candidate FZHW without a moveout trend across the JF array are rejected as false detections. This is followed by HPM analysis to confirm the existence of significant rotation between the polarization directions of the first and second phases in the early P waveforms.

3.3.2 *Results*

Applying the automatic detection algorithm of Ross & Ben-Zion (2014) on earthquakes that are within 10 km from the fault (black

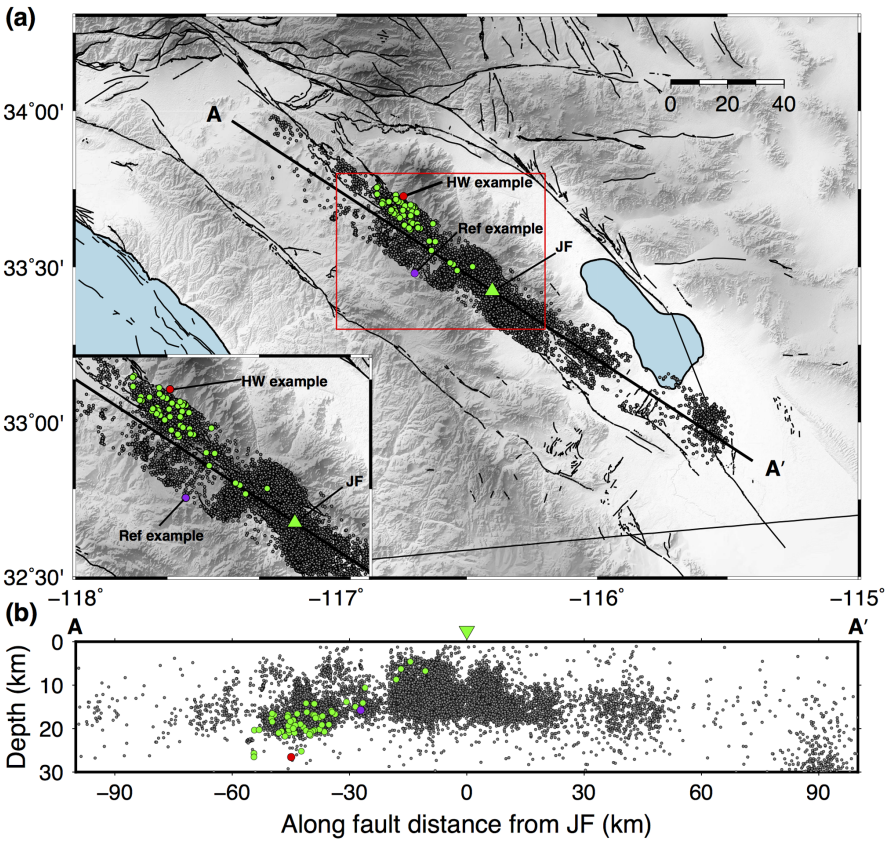

Figure 11. (a) Location map of 18 581 earthquakes (circles) used in the FZHW study (outlined by the purple box in Fig. 1). Green and red circles denote candidate events producing FZHW flagged through a combination of automatic detection and visual inspection. Data from an FZHW candidate event (red circle) and a reference event (purple circle) are compared in later figures. The region outlined by the red box is zoomed-in at the bottom left inset. (b) Depth section of hypocentres projected along the cross-session AA′ in (a).

line AA′ in Fig. 11) leads to numerous candidate FZHW. About 3000 events produce automatic detections in at least one JF station and about 1600 events produce detection in more than one station. The tentative detected phases are inspected visually and examined with HPM analysis to yield a high-quality data set of FZHW.

Waveforms with automatic FZHW picks at multiple stations are aligned on the *P* picks made at the onset of the earliest impulsive arrival. Figs 12(a) and (b) show example waveforms at stations of the JF array without and with FZHW. In Fig. 12(a), the first arrivals are standard impulsive *P* body waves (red triangles), while in Fig. 12(b) waveforms at stations JFN4–JFS2 start with emergent tentative FZHW (green squares) followed by larger amplitude sharper *P* body waves (red triangles). The moveout between the candidate FZHW and direct *P* arrivals in Fig. 12(b) decreases from NE to SW within the JF array, suggesting that the velocity contrast interface is on the NE side of the array.

To verify that the emergent early arrivals are not part of the direct *P* waves, we analyse the HPM of the early *P* waveforms. This is illustrated in Figs 13(a) and (b) using the example waveforms of Fig. 12 at station JFS1. The top panels of Fig. 13(a) display HPM trajectories for successive 0.1 s windows of 0.8 s in the early *P* waveform centred at the direct *P* arrival (red triangle in Fig. 13a, bottom). The azimuth and amplitude ratio between the successive subwindows of the HPM polarization are marked in the top panels. In this example with no FZHW, the amplitude ratio becomes very large only at the first window that includes the direct *P* arrival, and the HPM becomes polarized in the general horizontal direction of the body wave near the array. In a waveform that includes FZHW,

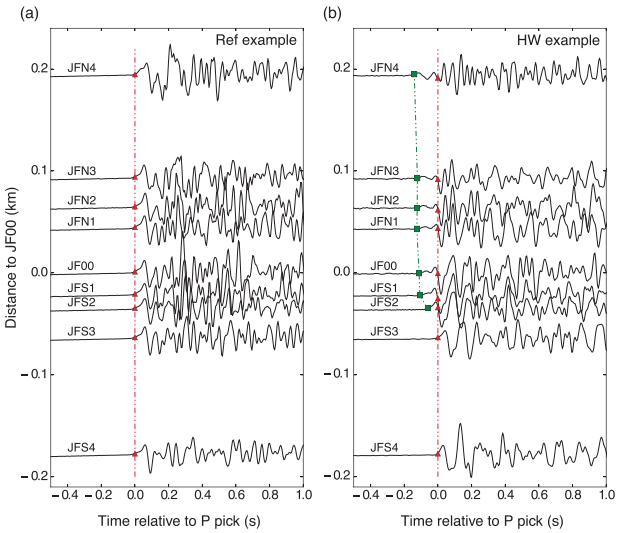

Figure 12. (a) Velocity seismograms of early *P* waveform at the JF array generated by the reference event denoted by the purple circle in Fig. 11. The waveforms are aligned on the automatic *P* picks (red triangles). (b) Same as (a) for the candidate event shown as the red circle in Fig. 11. The green squares indicate the automatic FZHW picks.

however, two windows with large amplitude ratios are observed in the HPM trajectories (top panels in Fig. 13b). The first window with a large amplitude change reflects the transition from noise to FZHW (green square in Fig. 13b, bottom), and the second window

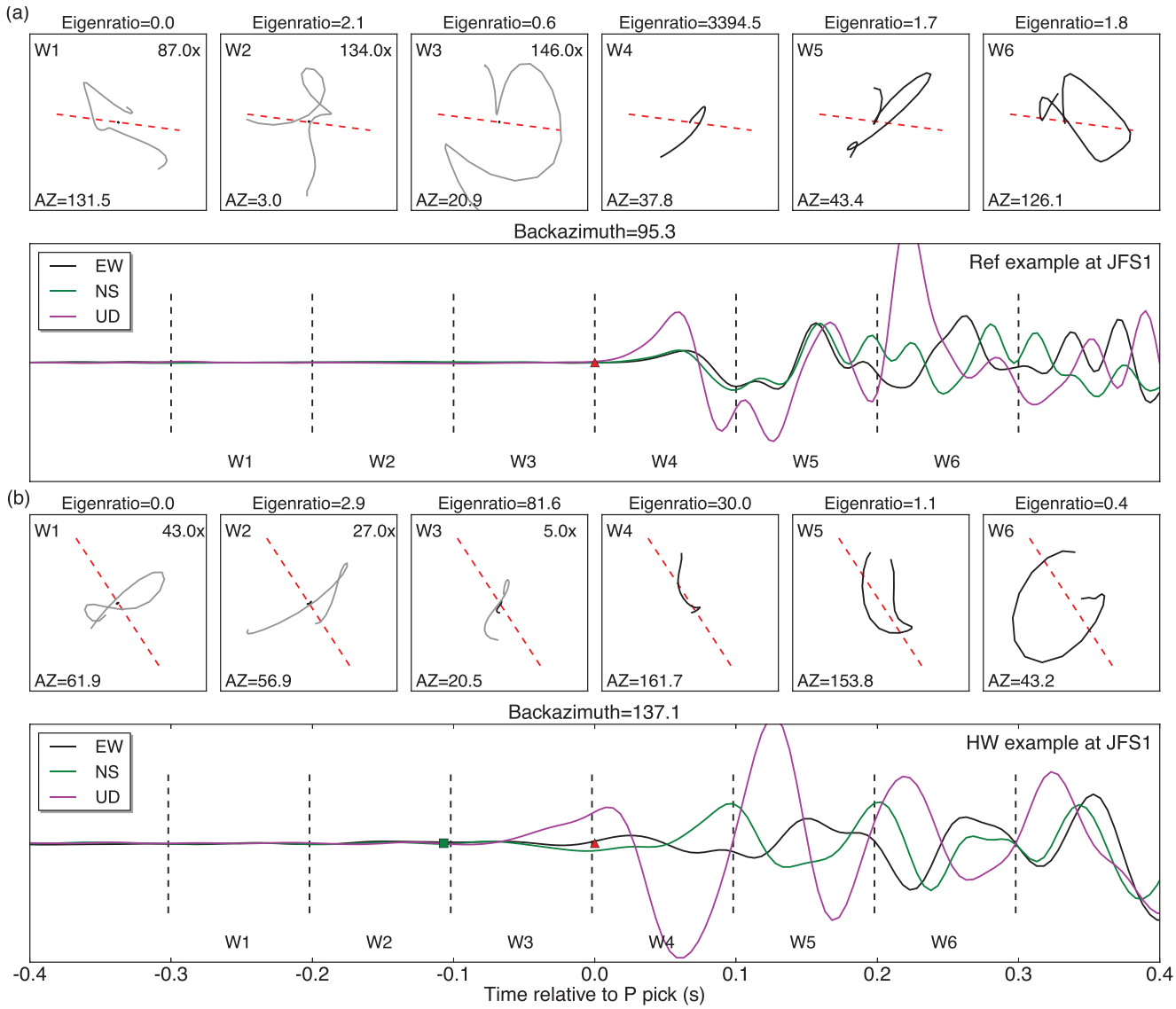

Figure 13. (a) Particle motion analysis on displacement seismograms at station JFS1 generated by the reference event. The early *P* waveforms centred at the automatic *P* pick (red triangle) for horizontal and vertical components are shown in green, black and purple in the bottom panel, respectively. The signal is cut into six blocks with equal length by the black dashed lines. The trajectory of horizontal particle motion in each block is depicted as the grey curve and compared with the backazimuth of the event (red dashed line) in the corresponding top panel. The trajectory is magnified in the first three windows with the amplification factor specified at the top right of the panel. For each signal block, eigenvalue ratio and backazimuth are computed through polarization analysis used in Bulut *et al*. (2012). (b) Same as (a) for the FZHW candidate event. The green square denotes the automatic FZHW pick.

accompanied also by a significant rotation of the polarization direction reflects the transition from FZHW to direct *P* phase.

Similar analyses lead to identification of 61 earthquakes, all located NW of the array (green and red circles in Fig. 11), that produce clear FZHW at multiple JF stations. To estimate properties of the velocity contrast interface that produce these FZHWs, we align the early *P* waveforms at station JF00 generated by the 61 earthquakes on the direct *P* arrival and plot them with increasing hypocentre distance (Fig. 14a). The moveout between the FZHW (green squares) and direct *P* arrivals (red triangle) is constant for a wide range of hypocentre distances (10–60 km). The constant moveout implies that the FZHWs observed at the JF array are generated by a local bimaterial interface, which may be associated with edge of the fault damage zone or basin, rather than a deep fault interface (Najdahmadi *et al*. 2016). Assuming that the length of the interface at the edge of a damage zone is 3.5–5 km, as suggested by the trapped waves analysis discussed next, leads to an estimated *P*-wave velocity contrast of 10.7–14.6 per cent (eq. 8a) using a 6 km s^{-1} average *P*-wave velocity outside the damage zone. The short propagation distance along the bimaterial interface explains (eq. 5) the rapid change in the moveout between FZHW and direct *P* arrival across stations of the JF array in Fig. 12(b), and the lack of FZHW at the SW most stations as shown in Fig. 14(b) for station JFS4.

3.4 Fault zone trapped waves

3.4.1 Methodology

FZTW result from constructive interference of critically reflected phases within a sufficiently uniform low-velocity fault zone layer (e.g. Ben-Zion & Aki 1990; Igel *et al*. 1997; Jahnke *et al*. 2002). The common type of FZTW is associated with the antiplane *S* case and is

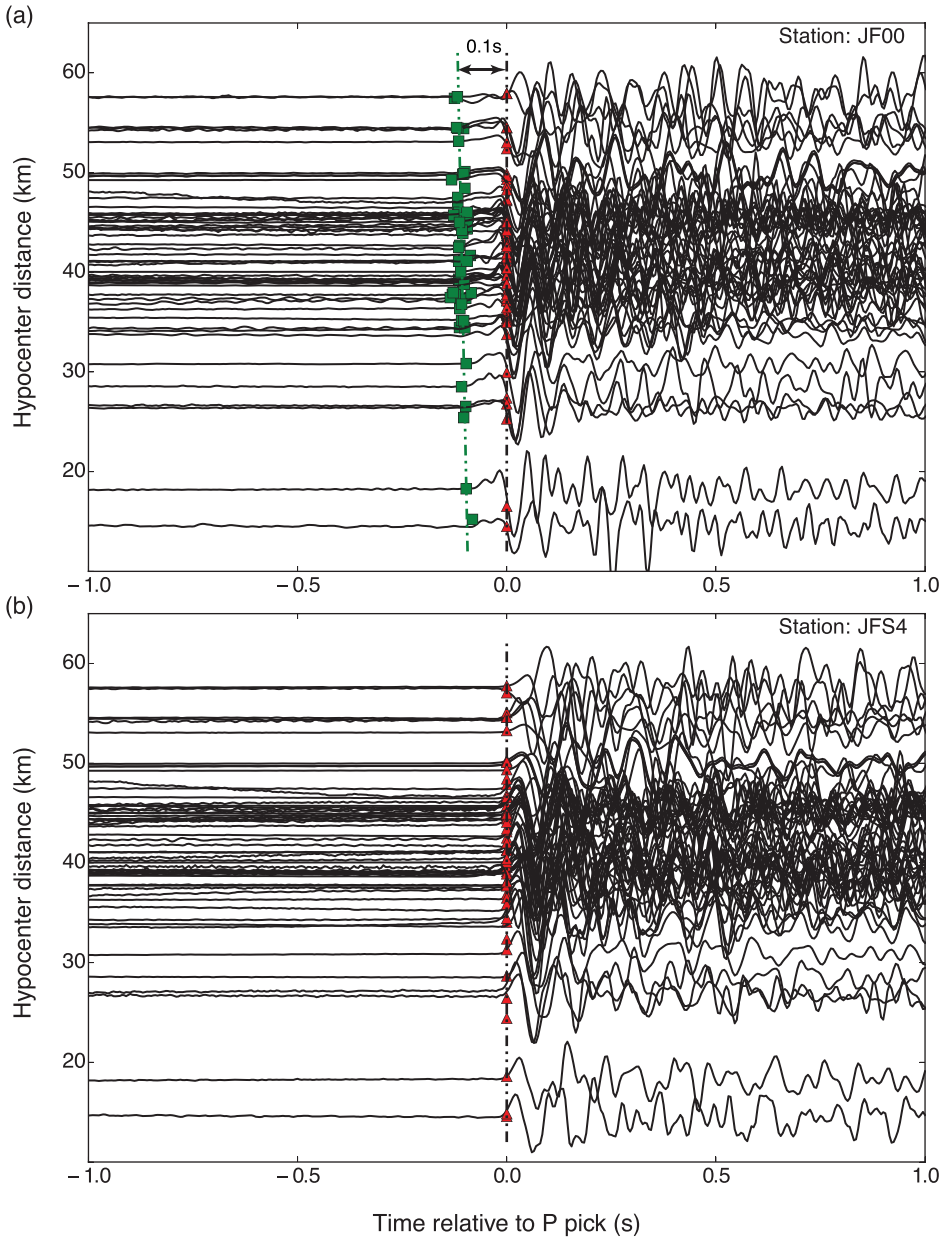

Figure 14. (a) Velocity seismograms recorded at station JF00 for FZHW candidate events marked by green and red circles in Fig. 11. The early *P* waveforms are aligned with the automatic direct *P* picks (red triangles) and plotted with increasing hypocentre distance. Green squares indicate candidate FZHW picks. Black and green dashed lines indicate zero time lag and best-fitting straight line crossing the green squares, respectively. A 0.1 s constant moveout between the green and black dashed lines is observed. (b) Same as (a) for the southwest end station JFS4. No FZHW are flagged.

analogous to surface Love waves of a horizontally layered structure. These waves follow the direct *S* wave, have relatively low frequencies, are at least somewhat dispersive and exist predominantly in the vertical and fault-parallel components of ground motion (Ben-Zion & Aki 1990). Additional types of FZTW are associated with Rayleigh-type resonance or leaky modes and appear between the *P* and *S* body waves (Ellsworth & Malin 2011). In this paper, we discuss observations and analysis of the more common Love type trapped waves following the direct *S* wave. We also observe possible candidates of Rayleigh or leaky type trapped waves, but these are less consistent (the waveform character and recording stations vary for different earthquakes) and are left for future work.

The amplitude, frequency content and duration of FZTW are very sensitive to combinations of internal fault zone properties including the width, velocity reduction, attenuation coefficient and propagation distance within the fault zone layer (Ben-Zion 1998). Observations and modeling of waveforms containing FZTW can provide high-resolution information on these properties (e.g. Li *et al*. 1990; Peng *et al*. 2003; Lewis *et al*. 2005; Mizuno & Nishigami 2006; Calderoni *et al*. 2012), although the modeling approach should account for the significant trade-offs between model parameters (Ben-Zion 1998; Jahnke *et al*. 2002; Lewis & Ben-Zion 2010).

Following the pre-processing steps suggested by Ross & Ben-Zion (2015), waveforms are first corrected for the instrument response, rotated to the fault-parallel component, and then bandpass filtered at 2–20 Hz. The detection of potential FZTW starts by applying the automated algorithm of Ross & Ben-Zion (2015) on the pre-processed data recorded at the JF array. The data flagged by the

automated algorithm are inspected visually to confirm the existence of resonance mode wave packages after the direct *S* arrivals that are observed consistently at a confined spatial range of the array.

Following Ben-Zion *et al*. (2003) and later studies, waveforms observed across the array that include FZTW at some stations are inverted for properties of the trapping structure using a genetic inversion algorithm with a forward kernel based on the 2-D analytical solution of Ben-Zion & Aki (1990) and Ben-Zion (1998). The analytical solution accounts for multiple plane-parallel fault zone layers between two quarter spaces. However, in this paper we find that a model configuration consisting of a single fault zone layer in a half-space (Fig. S5, Supporting Information) is sufficient to fit well the observed FZTW. This simple model has six key parameters that are perturbed in the inversion. The fault zone parameters consist of attenuation coefficient (Q_{FZ}), *S*-wave velocity (β_{FZ}), propagation distance (z_s) within the fault zone, width (W) and location of the fault zone layer (x) within the array. The host rock parameters are *S*-wave velocity (β_H) and attenuation coefficient (Q_H). The latter is fixed to be 400, which is the average value for Southern California (Hauksson & Shearer 2006), to reduce somewhat the number of parameters. The genetic inversion algorithm explores systematically the trade-offs between these model parameters. The propagation time of *S* waves outside the fault zone layer is an additional parameter used to check consistency of the results with the overall distances between the generating earthquakes and JF array.

To obtain a good estimation of the FZ parameters, 10 000 models with 50 generations and 200 models per generation are tested in each inversion. A successful inversion includes both good waveform fits, and agreement between parameters of the best-fitting model and peaks of the probability density distributions of parameters generated in the inversion process. As in Ben-Zion *et al*. (2003) and later related studies, prior to the inversion the fault-parallel seismograms are integrated to displacement and convolves with $1/t^{1/2}$ to convert a point source response to that of an equivalent line dislocation source (e.g. Vidale *et al*. 1985; Igel *et al*. 2002). Additional details on the method can be found in Ben-Zion *et al*. (2003).

3.4.2 Results

As discussed in Ross & Ben-Zion (2015), applying the automatic detection algorithm to the JF array data recorded during 2013 produced a total of 582 candidates FZTW with 90 per cent of the detections concentrated between JF00–JFS3. This suggests persistent generation of FZTW by a narrow FZ layer beneath stations JF00–JFS3 of the JF array. To focus on high-quality candidate FZTW, we apply the automatic detection algorithm on 28 995 earthquakes that are within 50 km from the fault using a higher detection threshold than Ross & Ben-Zion (2015). This leads to detection of trapped waves at stations JF00–JFS3 with an evaluation score >6.0 generated by 205 events (coloured circles in Fig. 15). The evaluation

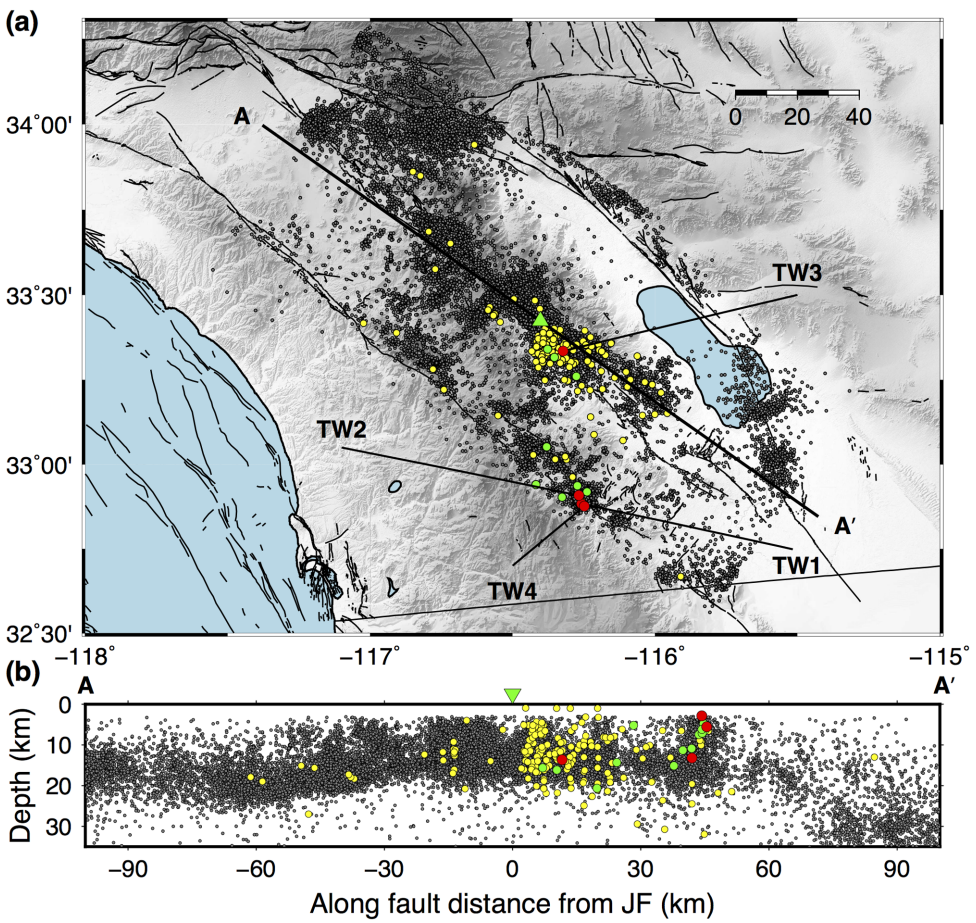

Figure 15. (a) Location map for earthquakes that are analysed for the presence of FZTW. Events flagged as generating high-quality FZTW are displayed as red, green and yellow circles. Seismograms of events denoted by green and red circles are used for moveout analysis (Fig. 16). Waveforms from events marked by red circles are inverted for structural parameters (Fig. 17 and Figs S7 and S8, Supporting Information). (b) Depth section of hypocentres projected along the cross-session AA′ in (a).

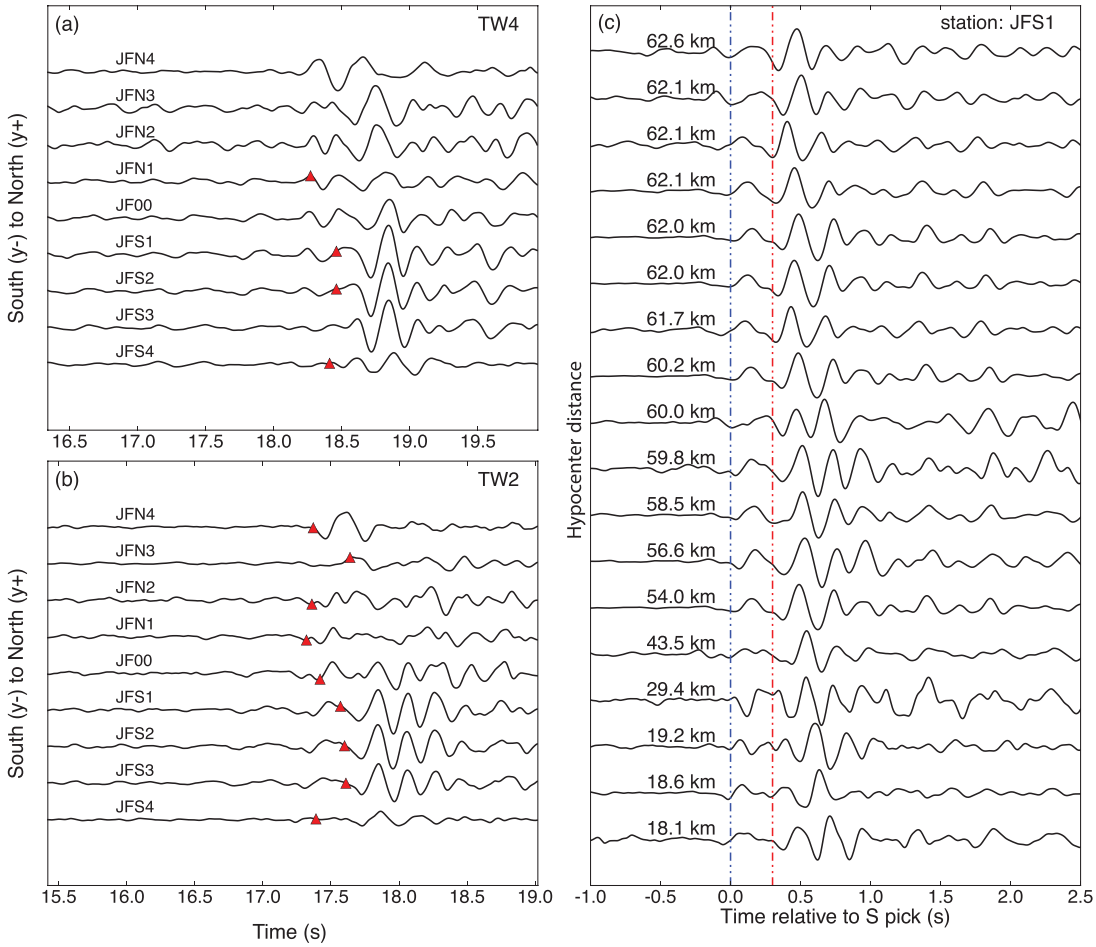

Figure 16. (a) Fault-parallel displacement seismograms generated by event TW4 (see location in Fig. 15). The waveforms are pre-processed following the steps illustrated in Fig. S6 in the Supporting Information. The red triangles denote the available automatic *S* picks. (b) Same as (a) for event TW2. (c) Displacement seismograms after pre-processing recorded at station JFS1 generated by events marked by green and red circles in Fig. 15. The *S* waveforms are aligned on the automatic *S* picks and plotted with increasing hypocentre distance indicated above each trace. The blue and red dashed lines denote the *S* and FZTW arrivals, respectively.

score is computed by summing up the *Y*-statistics described in Ross & Ben-Zion (2015). The detected phases in this high-quality data set are further visually inspected and evaluated. We note that many detections including those producing the clearest candidate FZTW (green and red circles) are generated by events located considerably away from the fault. This implies a relatively shallow trapping structure that can be excited by wave energy of regional events that enter the FZ layer from below (Ben-Zion *et al.* 2003; Fohrmann *et al*. 2004).

Fig. S6 in the Supporting Information illustrates the pre-processing steps performed on example event TW2. The direct *S*-wave picks are followed by resonance modes at stations JFS1–JFS3 that are especially clear on the displacement seismograms. Similar pre-processing and visual inspection indicate consistent large-amplitude resonance phases confined to stations JFS1–JFS3 for all 205 earthquakes producing high-quality FZTW. Figs 16 (a) and (b) display fault-parallel displacement waveforms across the JF array generated by example events TW2 and TW4 (see Fig. 15 for locations). The seismograms have clear FZTW at stations JFS1–JFS3 following the direct *S*-wave picks (red triangle). Waveforms generated by 18 earthquakes (green circles in Fig. 15) with clear and representative FZTW are used for further analysis. To estimate the overall scale of the trapping structure, we align the early *S* waveforms generated by the 18 earthquakes at station JFS1 on the direct *S* arrival, and arrange them with increasing hypocentre distance (Fig. 16c). The moveout between the direct *S* arrivals (blue dashed line) and FZTW (red dashed line) is constant for a wide range of hypocentre distance (20–60 km). This constant moveout supports the inference based on the regional distribution of events generating FZTW that the trapping structure below the JF array is relatively shallow.

Fig. 17 presents inversion results for the displacement seismograms at the JF array generated by earthquakes TW1 and TW4. As the distance between the hypocentres of TW1 and TW4 is ∼2 km, the waveforms generated at each station by the two earthquakes are stacked to increase the SNR. Performing inversions for waveforms generated by each event separately lead to very similar results to those discussed below. Fig. 17(a) compares synthetic waveforms associated with the best-fitting model (green lines) and observed seismograms (black lines). Fig. 17(b) presents fitness values calculated by the genetic inversion algorithm for different FZ parameters. The fitness for a given set of parameters is defined as $(1+C)/2$, where C is the cross-correlation coefficient between the set of synthetic and observed waveforms at all stations. The thin curves in Fig. 17(b) give probability density functions for the various model parameters, calculated by summing the fitness values of the final 2000

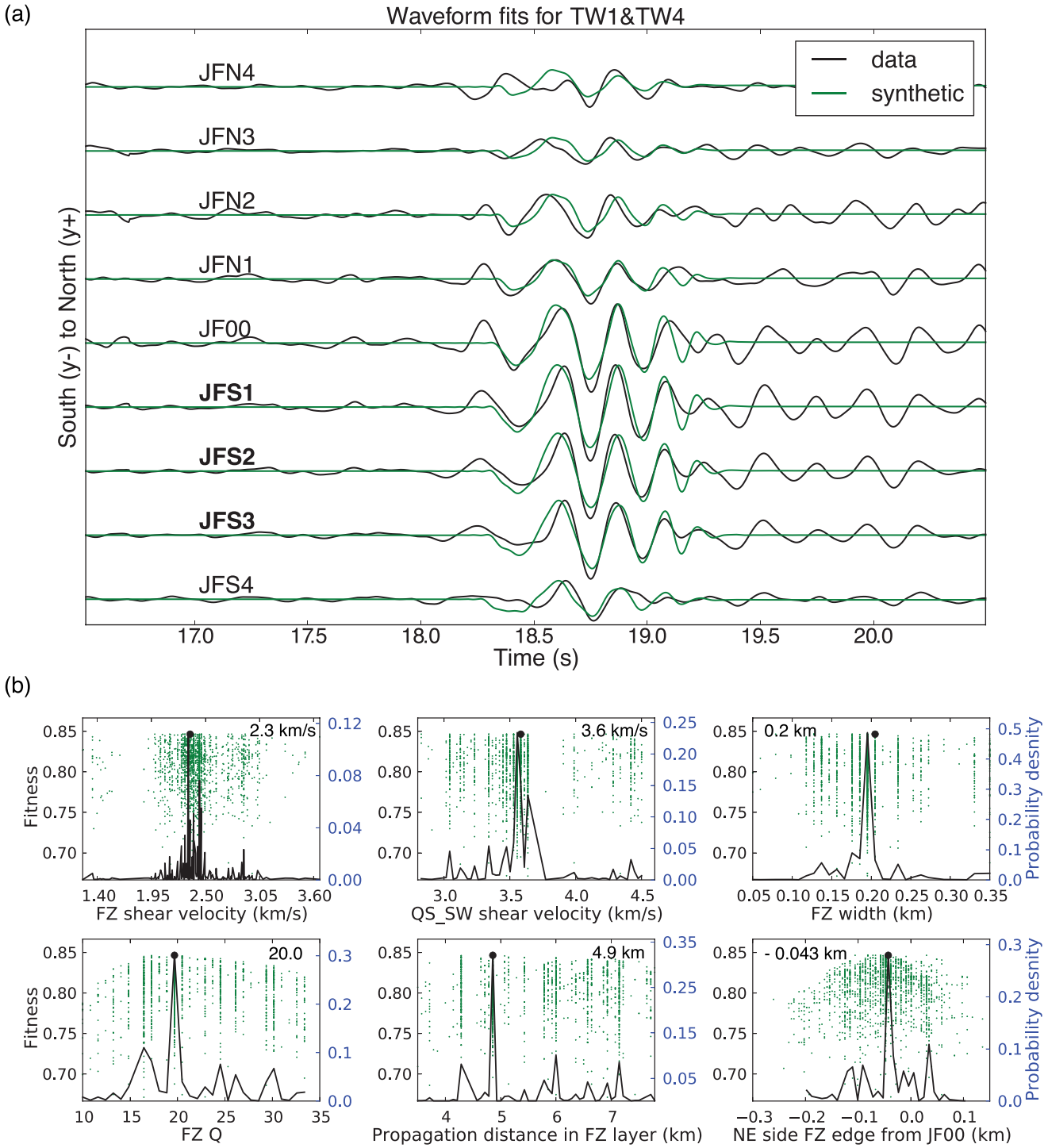

Figure 17. Inversion results modeling stacked displacement seismograms at the JF array generated by candidate events TW1 and TW4. (a) Comparison between the observed (black) and synthetic (green) seismograms. (b) Fitness values (green dots) calculated for different FZ parameters tested in the inversion. The parameters associated with the best-fitting model (black circles) are displayed in each panel and used to produce the synthetic waveforms shown in (a). The black curves indicate probability density functions for the inverted model parameters.

inversion iterations and normalizing the results to have unit sums. The parameter values associated with the best-fitting model (black dots) are very close to the peaks of the probability density functions. The close waveform fits in Fig. 17(a) and the results in Fig. 17(b) imply convergent and robust inversion results. The best-fitting parameters indicate that the trapping structure below the JF array has width of ∼200 m, length scale of ∼5 km, Q_S of ∼20 and *S*-wave velocity reduction of ∼35 per cent compared to the host rock. The ∼5 km propagation distance along the waveguide is associated with a combination of along-strike and vertical components. Assuming for simplicity that the average along-strike and vertical components are the same (Ben-Zion *et al*. 2003), the depth of the trapping FZ

layer is ∼3.5 km. Figs S7 and S8 in the Supporting Information show inversion results of FZTW generated by earthquakes TW2 and TW3. The best-fitting parameters and peaks of the probability density functions are similar to those shown in Fig. 17.

4 DISCUSSION

We use delay times of *P* waves from local and teleseismic earthquakes, FZHW and FZTW to image the internal structure of the Clark fault at the JF site in the trifurcation area of the SJFZ. The identification of the various phases is done first with automated detection algorithms (Ross & Ben-Zion 2014, 2015) enabling systematic and objective analyses of large data sets (∼29 000 events recorded at nine stations). This is followed by visual inspection of detected phases augmented by some additional analysis (e.g. examining the HPM of candidate head waves) to substantiate the validity of the automatic detections. These procedures lead to identification of >60 near-fault events producing early *P* arrivals at multiple stations of the JF array with characteristics of FZHW (Fig. 11), >200 broadly distributed events producing high-quality FZTW at stations JF00–JFS3 (Fig. 15), and *P* body wave arrivals from ∼3500 earthquakes in the region around the SJFZ (Fig. 1).

Teleseismic *P* waves in the frequency range of 0.01–0.5 Hz observed at the JF and TR arrays indicate faster seismic velocities beneath the TR array compared to the JF array, in contrast with the expectation from the larger scale tomography results (Fig. 3). The reversal of seismic velocities near the fault points to a prominent local LVZ underneath the JF array. This is supported by both the teleseismic *P*-wave delay time derived from the frequency range 0.2–0.5 Hz and statistical analysis of the *P*-wave delay times associated with numerous local events. Some of the velocity reduction below the JF array is related to the fact that it is located in a local basin with sediments. However, the basin is part of the fault zone structure (e.g. Sibson 1986; Ben-Zion *et al*. 2003) and it includes an inner LVZ that forms a seismic trapping structure. Assuming that the average *P*-wave velocity of the host rock is ∼6 km s^{-1} (Fig. 3) and that the LVZ beneath the JF array has ∼20 per cent velocity reduction in the top 3.5 km (based on the velocity contrast indicated by the FZHW and some additional reduction in the more intense inner damage zone producing FZTW), a vertical incident *P* wave is delayed beneath the JF array by ∼0.15 s compared to the TR array. This is sufficient to reverse the traveltime variation that may be produced by the larger scale deeper structures shown in Fig. 3. The delay time results also suggest that the main seismogenic fault is between stations JF3 and JF4. This is consistent with a prominent large-scale geomorphologic feature in this section of the fault (Fig. 18).

The observation of a constant moveout between FZHW and direct *P* phases indicates that the FZHW are generated by a local velocity contrast, inferred to be at the edge of the LVZ on the NE side of the JF array. This is confirmed by the fact that the observed 0.1 s constant FZHW–*P* moveout implies a 10–15 per cent contrast of *P*-wave velocities across the bimaterial interface, which is larger than any deep velocity contrast interface found in previous studies at various faults (e.g. Zhao *et al*. 2010; Yang *et al*. 2015; Najdahmadi *et al*. 2016; Share & Ben-Zion 2016). The LVZ beneath the JF array contains a narrower damage zone concentrated below stations JFS1–JFS3 generating clear FZTW. Inversions of sets of waveforms observed across the JF array with high-quality FZTW at stations JFS1–JFS3 indicate (Fig. 17 and Figs S7 and S8, Supporting Information) that the trapping structure is ∼200 m wide and has V_S reduction of ∼30–40 per cent, Q_S of ∼20 and depth of ∼3.5 km. The relatively shallow depth of the trapping structure is supported by (Fig. 15) the wide distribution of events generating FZTW (e.g. Fohrmann *et al*. 2004) and the constant moveout (Fig. 16) between the direct *S* and trapped waves (e.g. Ben-Zion *et al*. 2003; Peng *et al*. 2003). These results are similar to properties estimated from analysis of FZ-reflected phases at the JF array (Yang *et al*. 2014), as

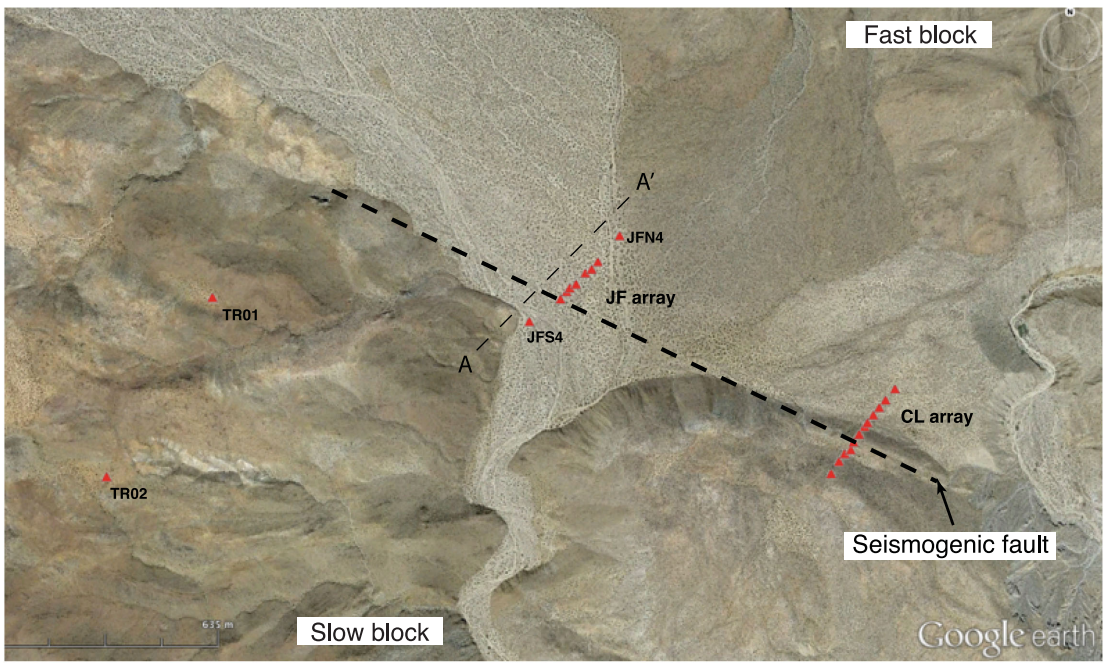

Figure 18. Google Earth map view of a 2.5 × 2 km region centred at the JF array. The red triangles denote stations of the JF and CL arrays with additional two stations of the TR array. The black dashed thick line parallel to the fault strike indicates the estimated location of seismogenic fault. The blocks to the NE and SW of the fault are marked as fast and slow based on previous tomography results (Fig. 3). A fault zone model along cross-session AA′ integrating the analysis results is shown in Fig. 19.

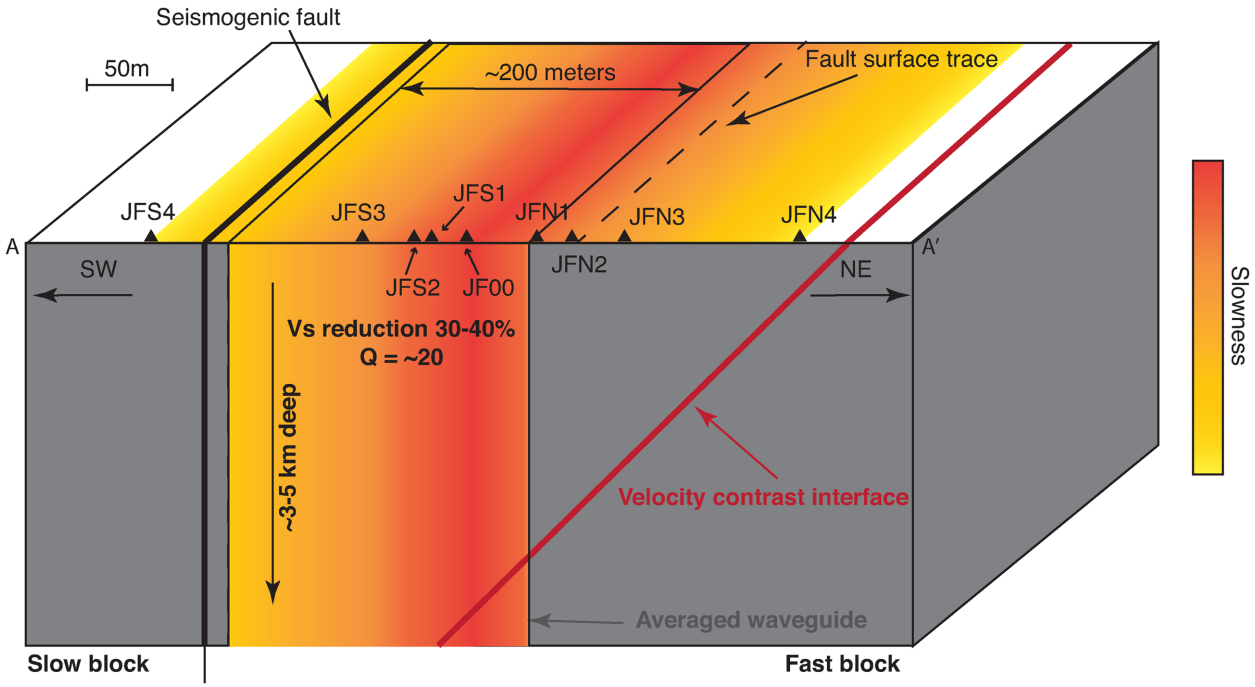

Figure 19. A conceptual model for fault zone structure at the JF site along the cross-session AA′ in Fig. 18. The lower velocities beneath stations JFS3–JFN2 (warmer colours) are indicated by delay times of teleseismic and local *P* waves. The red thick line denotes a local bimaterial interface that generates FZHW (Section 3.3). A fault zone waveguide is depicted by a vertical layer with NE boundary located at JFN1. The marked S wave *Q*, velocity reduction, width and depth of the waveguide are constrained by waveform inversions (Section 3.4). The inferred seismogenic fault crosses the JF array between stations JFS3 and JFS4.

well as analysis of FZTW and FZ-reflected phases at the CL array deployed across the Clark fault about 1 km to the SE from the JF array in 1999 (Li & Vernon 2001; Lewis *et al*. 2005; Yang & Zhu 2010). We note that Li & Vernon (2001) suggested that the trapping structure below the CL array extends to a depth of ∼18 km, but this has been disputed by later analyses (Lewis *et al*. 2005; Yang & Zhu 2010).

Fig. 19 provides a schematic summary of the different imaging results done in this work, with a focus on the structure below the dense JF array. The seismogenic fault is inferred to be located between stations JFS3 and JFS4 and is associated with a strongly asymmetric LVZ that exists primary on the NE side of the fault. A similar asymmetric LVZ was observed at the nearby CL array (Lewis *et al*. 2005; Yang & Zhu 2010), and in larger scale analysis of geomorphologic features in the area (Wechsler *et al*. 2009). The offset of rock damage across the fault to the side with faster velocities at seismogenic depth (Fig. 3) may be produced by preferred propagation direction of earthquake ruptures in the area to the NW (e.g. Ben-Zion & Shi 2005; Xu *et al*. 2012). This is consistent with rupture directivities of small events (Kurzon *et al*. 2014) and along-strike asymmetry of stacked aftershock sequences in the area (Zaliapin & Ben-Zion 2011).

The results of this paper are based on data recorded across the Clark fault at one location. The SJFZ has heterogeneous structures with significant along-strike variations of the surface geology (e.g. Sharp 1967), seismicity (e.g. Hauksson *et al*. 2012), interseismic strain rates (e.g. Wdowinski 2009; Lindsey & Fialko 2013) and large-scale seismic velocities (e.g. Allam *et al*. 2014a; Zigone *et al*. 2015). Yang *et al*. (2014) and Li *et al*. (2015) documented along-strike variations of local damage zones and seismic anisotropy using data recorded by the various linear arrays across the SJFZ (triangles in Fig. 1). Several studies are currently underway on detailed analyses of the type done in this work using data recorded by the other dense linear arrays.

ACKNOWLEDGEMENTS

The study was supported by the National Science Foundation (grant EAR-162061) and the U.S. Department of Energy (awards DE-SC0016520 and DE-SC0016527). We thank the Anza-Borrego Desert State Park for permission to collect data on Jackass Flat. The seismic instruments were provided by the Incorporated Research Institutions for Seismology (IRIS) through the PASSCAL Instrument Center at New Mexico Tech. Data collected are available through the IRIS Data Management Center. The facilities of the IRIS Consortium are supported by the National Science Foundation under Cooperative Agreement EAR-1261681 and the DOE National Nuclear Security Administration. The manuscript benefitted from comments by two anonymous referees.

REFERENCES

Allam, A.A. & Ben-Zion, Y., 2012. Seismic velocity structures in the Southern California plate-boundary environment from double-difference tomography, *Geophys. J. Int.,* **190**(2), 1181–1196.

Allam, A.A., Ben-Zion, Y., Kurzon, I. & Vernon, F., 2014a. Seismic velocity structure in the Hot Springs and Trifurcation Areas of the San Jacinto fault zone, California, from double-difference tomography, *Geophys. J. Int.,* **198**(2), 978–999.

Allam, A.A., Ben-Zion, Y. & Peng, Z., 2014b. Seismic imaging of a bimaterial interface along the Hayward fault, CA, with fault zone head waves and direct P arrivals, *Pure appl. Geophys.,* **171**(11), 2993–3011.

Ampuero, J.P. & Ben-Zion, Y., 2008. Cracks, pulses and macroscopic asymmetry of dynamic rupture on a bimaterial interface with velocity-weakening friction, *Geophys. J. Int.,* **173**(2), 674–692.

Ben-Zion, Y., 1989. The response of two joined quarter spaces to SH line sources located at the material discontinuity interface, *Geophys. J. Int.,* **98**(2), 213–222.

Ben-Zion, Y., 1990. The response of two half spaces to point dislocations at the material interface, *Geophys. J. Int.,* **101**(3), 507–528.

Ben-Zion, Y., 1998. Properties of seismic fault zone waves and their utility for imaging low velocity structures, *J. geophys. Res.,* **103**(B6), 12567–12585.

Ben-Zion, Y. & Aki, K., 1990. Seismic radiation from an SH line source in a laterally heterogeneous planar fault zone, *Bull. seism. Soc. Am.,* **80**(4), 971–994.

Ben-Zion, Y. & Andrews, D.J., 1998. Properties and implications of dynamic rupture along a material interface, *Bull. seism. Soc. Am.,* **88**(4), 1085–1094.

Ben-Zion, Y. & Malin, P., 1991. San-Andreas fault zone head waves near Parkfield, California, *Science,* **251,** 1592–1594.

Ben-Zion, Y. & Huang, Y., 2002. Dynamic rupture on an interface between a compliant fault zone layer and a stiffer surrounding solid, *J. geophys. Res.,* **107**(B2), 2042, doi:10.1029/2001JB000254.

Ben-Zion, Y. & Sammis, C.G., 2003. Characterization of fault zones, *Pure appl. Geophys.,* **160**(3–4), 677–715.

Ben-Zion, Y. *et al.*, 2003. A shallow fault-zone structure illuminated by trapped waves in the Karadere–Duzce branch of the North Anatolian Fault, western Turkey, *Geophys. J. Int.,* **152**(3), 699–717.

Ben-Zion, Y. & Shi, Z., 2005. Dynamic rupture on a material interface with spontaneous generation of plastic strain in the bulk, *Earth planet. Sci. Lett.,* **236**(1), 486–496.

Brietzke, G.B. & Ben-Zion, Y., 2006. Examining tendencies of in-plane rupture to migrate to material interfaces, *Geophys. J. Int.,* **167**(2), 807–819.

Brietzke, G.B., Cochard, A. & Igel, H., 2009. Importance of bimaterial interfaces for earthquake dynamics and strong ground motion, *Geophys. J. Int.,* **178**(2), 921–938.

Bulut, F., Ben-Zion, Y. & Bohnhoff, M., 2012. Evidence for a bimaterial interface along the Mudurnu segment of the North Anatolian Fault Zone from polarization analysis of P waves, *Earth planet. Sci. Lett.,* **327,** 17–22.

Calderoni, G., Di Giovambattista, R., Vannoli, P., Pucillo, S. & Rovelli, A., 2012. Fault-trapped waves depict continuity of the fault system responsible for the 6 April 2009 M_w 6.3 L'Aquila earthquake, central Italy, *Earth planet. Sci. Lett.,* **323,** 1–8.

Cochran, E.S., Li, Y., Shearer, P.M., Barbot, S., Fialko, Y. & Vidale, J.E., 2009. Seismic and geodetic evidence for extensive, long-lived fault damage zones, *Geology,* **37,** 315–318.

Crotwell, H.P., Owens, T.J. & Ritsema, J., 1999. The TauP Toolkit: flexible seismic travel-time and ray-path utilities, *Seismol. Res. Lett.,* **70**(2), 154–160.

Dor, O., Rockwell, T.K. & Ben-Zion, Y., 2006. Geological observations of damage asymmetry in the structure of the San Jacinto, San Andreas and Punchbowl faults in Southern California: a possible indicator for preferred rupture propagation direction, *Pure appl. Geophys.,* **163**(2–3), 301–349.

Dor, O., Yildirim, C., Rockwell, T.K., Ben-Zion, Y., Emre, O., Sisk, M. & Duman, T.Y., 2008. Geological and geomorphologic asymmetry across the rupture zones of the 1943 and 1944 earthquakes on the North Anatolian Fault: possible signals for preferred earthquake propagation direction, *Geophys. J. Int.,* **173**(2), 483–504.

Ellsworth, W.L. & Malin, P.E., 2011. Deep rock damage in the San Andreas Fault revealed by P-and S-type fault-zone-guided waves, *Geol. Soc. Lond. Spec. Publ.,* **359**(1), 39–53.

Fay, N.P. & Humphreys, E.D., 2005. Fault slip rates, effects of elastic heterogeneity on geodetic data, and the strength of the lower crust in the Salton Trough region, southern California, *J. geophys. Res.,* **110**(B9), doi:10.1029/2004JB003548.

Fohrmann, M., Igel, H., Jahnke, G. & Ben-Zion, Y., 2004. Guided waves from sources outside faults: an indication for shallow fault zone structure?, *Pure appl. Geophys.,* **161,** 2125–2137.

Hauksson, E. & Shearer, P.M., 2006. Attenuation models (QP and QS) in three dimensions of the southern California crust: inferred fluid saturation at seismogenic depths, *J. geophys. Res.,* **111**(B5), doi:10.1029/2005JB003947.

Hauksson, E., Yang, W. & Shearer, P.M., 2012. Waveform relocated earthquake catalog for southern California (1981 to June 2011), *Bull. seism. Soc. Am.,* **102**(5), 2239–2244.

Hough, S.E., Ben-Zion, Y. & Leary, P., 1994. Fault-zone waves observed at the southern Joshua Tree earthquake rupture zone, *Bull. seism. Soc. Am.,* **84**(3), 761–767.

Huang, Y., Ampuero, J.-P. & Helmberger, D.V., 2014. Earthquake ruptures modulated by waves in damaged fault zones, *J. geophys. Res.,* **119,** 3133–3154.

Igel, H., Ben-Zion, Y. & Leary, P.C., 1997. Simulation of SH-and P-SV-wave propagation in fault zones, *Geophys. J. Int.,* **128**(3), 533–546.

Igel, H., Jahnke, G. & Ben-Zion, Y., 2002. Numerical simulation of fault zone guided waves: accuracy and 3-D effects, *Pure appl. Geophys.,* **159,** 2067–2083.

Jahnke, G., Igel, H. & Ben-Zion, Y., 2002. Three-dimensional calculations of fault-zone-guided waves in various irregular structures, *Geophys. J. Int.,* **151**(2), 416–426.

Kennett, B.L.N. & Engdahl, E.R., 1991. Travel times for global earthquake location and phase identification, *Geophys. J. Int.,* **105**(2), 429–465.

Kissling, E., 1988. Geotomography with local earthquake data, *Rev. Geophys.,* **26**(4), 659–698.

Kurzon, I., Vernon, F.L., Ben-Zion, Y. & Atkinson, G., 2014. Ground motion prediction equations in the San Jacinto fault zone: significant effects of rupture directivity and fault zone amplification, *Pure appl. Geophys.,* **171**(11), 3045–3081.

Lewis, M.A., Peng, Z., Ben-Zion, Y. & Vernon, F.L., 2005. Shallow seismic trapping structure in the San Jacinto fault zone near Anza, California, *Geophys. J. Int.,* **162**(3), 867–881.

Lewis, M.A. & Ben-Zion, Y., 2010. Diversity of fault zone damage and trapping structures in the Parkfield section of the San Andreas Fault from comprehensive analysis of near fault seismograms, *Geophys. J. Int.,* **183**(3), 1579–1595.

Li, Y.-G., Leary, P.C., Aki, K. & Malin, P.E., 1990. Seismic trapped modes in the Oroville and San Andreas fault zones, *Science,* **249,** 763–766.

Li, Y.G. & Vernon, F.L., 2001. Characterization of the San Jacinto fault zone near Anza, California, by fault zone trapped waves, *J. geophys. Res.,* **106**(B12), 30 671–30 688.

Li, Z., Peng, Z., Ben-Zion, Y. & Vernon, F.L., 2015. Spatial variations of shear-wave anisotropy near the San Jacinto fault zone in Southern California, *J. geophys. Res.,* **120,** 8334–8347.

Lindsey, E.O. & Fialko, Y., 2013. Geodetic slip rates in the southern San Andreas fault system: effects of elastic heterogeneity and fault geometry, *J. geophys. Res.,* **118**(2), 689–697.

McGuire, J. & Ben-Zion, Y., 2005. High-resolution imaging of the Bear Valley section of the San Andreas Fault at seismogenic depths with fault-zone head waves and relocated seismicity, *Geophys. J. Int.,* **163**(1), 152–164.

Mizuno, T. & Nishigami, K., 2006. Deep structure of the Nojima Fault, southwest Japan, estimated from borehole observations of fault-zone trapped waves, *Tectonophysics,* **417**(3), 231–247.

Najdahmadi, B., Bohnhoff, M. & Ben-Zion, Y., 2016. Bimaterial interfaces at the Karadere segment of the North Anatolian Fault, northwestern Turkey, *J. geophys. Res.,* **121,** 931–950.

Olsen, K.B., 2006. Strong shaking in Los Angeles expected from southern San Andreas earthquake, *Geophys. Res. Lett.,* **33**(7), doi:10.1029/2005GL025472.

Onderdonk, N.W., Rockwell, T.K., McGill, S.F. & Marliyani, G.I., 2013. Evidence for seven surface ruptures in the past 1600 years on the Claremont fault at Mystic Lake, northern San Jacinto fault zone, California, *Bull. seism. Soc. Am.,* **103**(1), 519–541.

Ozakin, Y., Ben-Zion, Y., Aktar, M., Karabulut, H. & Peng, Z., 2012. Velocity contrast across the 1944 rupture zone of the North Anatolian fault east of Ismetpasa from analysis of teleseismic arrivals, *Geophys. Res. Lett.,* **39**(8), L08307, doi:10.1029/2012GL051426.

Peng, Z., Ben-Zion, Y., Michael, A.J. & Zhu, L., 2003. Quantitative analysis of seismic fault zone waves in the rupture zone of the 1992 Landers, Cal-

ifornia, earthquake: evidence for a shallow trapping structure, *Geophys. J. Int.,* **155**(3), 1021–1041.
Petersen, M.D. & Wesnousky, S.G., 1994. Fault slip rates and earthquake histories for active faults in southern California, *Bull. seism. Soc. Am.,* **84**(5), 1608–1649.
Rockwell, T.K., Dawson, T.E., Young Ben-Horin, J. & Seitz, G., 2015. A 21-event, 4,000-year history of surface ruptures in the Anza Seismic Gap, San Jacinto Fault and implications for long-term earthquake production on a major plate boundary fault, *Pure appl. Geophys.,* **172**(5), 1143–1165.
Ross, Z.E. & Ben-Zion, Y., 2014. Automatic picking of direct P, S seismic phases and fault zone head waves, *Geophys. J. Int.,* **199**(1), 368–381.
Ross, Z.E. & Ben-Zion, Y., 2015. An algorithm for automated identification of fault zone trapped waves, *Geophys. J. Int.,* **202**(2), 933–942.
Ross, Z.E., White, M.C., Vernon, F.L. & Ben-Zion, Y., 2016. An improved algorithm for real time S-wave picking with application to the (Augmented) ANZA seismic network in southern California, *Bull. seism. Soc. Am.,* **106**(5), 2013–2022.
Rowe, C.D. & Griffith, W.A., 2015. Do faults preserve a record of seismic slip: a second opinion. Invited Review, *J. Struct. Geol.,* **78,** 1–26.
SCEDC, 2013. Southern California Earthquake Data Center, Caltech Dataset, doi:10.7909/C3WD3xH.
Share, P.E. & Ben-Zion, Y., 2016. Bimaterial interfaces in the South San Andreas Fault with opposite velocity contrasts NW and SE from San Gorgonio Pass, *Geophys. Res. Lett.,* **43,** 10 680–10 687.
Sharp, R.V., 1967. The San Jacinto fault zone in the Peninsular Ranges of southern California, *Bull. geol. Soc. Am..,* **78,** 705–730.
Shlomai, H. & Fineberg, J., 2016. The structure of slip-pulses and supershear ruptures driving slip in bimaterial friction, *Nat. Commun.,* **7,** 11787, doi:10.1038/ncomms11787.
Sibson, R.H., 1986. Rupture interaction with fault jogs, *Earthq. Source Mech.,* **37,** 157–167.
Vernon, F. & Ben-Zion, Y., 2010. *San Jacinto Fault Zone Experiment,* International Federation of Digital Seismograph Networks. Other/Seismic Network, doi:10.7914/SN/YN_2010.
Vidale, J., Helmberger, D.V. & Clayton, R.W., 1985. Finite-difference seismograms for SH waves, *Bull. seism. Soc. Am.,* **75**(6), 1765–1782.
Wdowinski, S., 2009. Deep creep as a cause for the excess seismicity along the San Jacinto fault, *Nat. Geosci.,* **2**(12), 882–885.
Wechsler, N., Rockwell, T.K. & Ben-Zion, Y., 2009. Analysis of rock damage asymmetry from geomorphic signals along the trifurcation area of the San-Jacinto Fault, *Geomorphology,* **113,** 82–96.
Weertman, J., 1980. Unstable slippage across a fault that separates elastic media of different elastic constants, *J. geophys. Res.,* **85**(B3), 1455–1461.
Weng, H., Yang, H., Zhang, Z. & Chen, X., 2016. Earthquake rupture extents and coseismic slips promoted by damaged fault zones, *J. geophys. Res.,* **121**(6), 4446–4457.
White, M.C.A., Ross, Z.E., Vernon, F.L. & Ben-Zion, Y., 2016. A detailed automatic 1998-2015 earthquake catalog of the San Jacinto fault zone region, in *Abstract of the Annual Meeting of the Southern California Earthquake Center*.
Xu, S., Ben-Zion, Y. & Ampuero, J.P., 2012. Properties of inelastic yielding zones generated by in-plane dynamic ruptures—II. Detailed parameter-space study, *Geophys. J. Int.,* **191**(3), 1343–1360.
Yang, H. & Zhu, L., 2010. Shallow low-velocity zone of the San Jacinto fault from local earthquake waveform modelling, *Geophys. J. Int.,* **183,** 421–432.
Yang, H., Li, Z., Peng, Z., Ben-Zion, Y. & Vernon, F., 2014. Low velocity zones along the San Jacinto Fault, Southern California, from body waves recorded in dense linear arrays, *J. geophys. Res.,* **119,** 8976–8990.
Yang, W., Peng, Z., Wang, B., Li, Z. & Yuan, S., 2015. Velocity contrast along the rupture zone of the 2010 M_w 6. 9 Yushu, China, earthquake from fault zone head waves, *Earth planet. Sci. Lett.,* **416,** 91–97.
Zaliapin, I. & Ben-Zion, Y., 2011. Asymmetric distribution of aftershocks on large faults in California, *Geophys. J. Int.,* **185,** 1288–1304.
Zhao, P. & Peng, Z., 2008. Velocity contrast along the Calaveras fault from analysis of fault zone head waves generated by repeating earthquakes, *Geophys. Res. Lett.,* **35**(1), doi:10.1029/2007GL031810.
Zhao, P., Peng, Z., Shi, Z., Lewis, M.A. & Ben-Zion, Y., 2010. Variations of the velocity contrast and rupture properties of M6 earthquakes along the Parkfield section of the San Andreas fault, *Geophys. J. Int.,* **180**(2), 765–780.
Zigone, D., Ben-Zion, Y., Campillo, M. & Roux, P., 2015. Seismic tomography of the Southern California plate boundary region from noise-based Rayleigh and Love waves, *Pure appl. Geophys.,* **172**(5), 1007–1032.

SUPPORTING INFORMATION

Supplementary data are available at *GJIRAS* online.

Figure S1. (a) Same as Fig 4(a). The red circle denotes event #1 analysed in the Supporting Information; the event information is shown in the title. (b) Spectrogram for the analysed event (same as Fig. 4c). (c) Same as Fig. 5(b) for the analysed event. (d) Same as Fig. 7(a) for the analysed event. (e) Same as Fig. 7(b) for the analysed event.
Figure S2. Same as Fig. S1 in the Supporting Information for event # 2 analysed in the Supporting Information.
Figure S3. (a) Location map and depth section of 3493 local earthquakes within the red box shown in Fig. 1(a), used in the local *P*-wave DTA to estimate relative slowness. (b) Same as (a) with events SW and NE of the fault denoted by red and green circles, respectively. (c) Same as (a) with events SE and NW of the JF array denoted by red and green circles, respectively. (d) Same as (a) with green (I), purple (II), red (III) and blue (IV) circles representing events west, north, east and south of the JF array, respectively.
Figure S4. (a) Mean values of the relative slowness computed for the 1434 events SW (red) and 2059 events NE (green) of the fault at the JF array. Same as Fig. 10(c); the black curve denotes the relative slowness for all 3493 events. Error bars indicate a range of two standard deviations about each respective mean value. (b) Same as (a) for 1132 events SE (red) and 2361 events NW (green) of the fault. (c) Same as (a) for 637, 1724, 797 and 335 events in quadrants I (green), II (purple), III (blue) and IV (red). Despite the variations between relative slowness calculated for events in different subsets, the shapes of the mean values remain similar.
Figure S5. A model for a vertical low-velocity fault zone layer in a half-space used in the inversion of fault zone trapped waves (Ben-Zion and Aki 1990; Ben-Zion 1998). The source is an *SH* line dislocation with coordinates (x_S, z_S). Width, quality factor and shear wave velocity are marked by W, Q and β, respectively. Subscripts H and FZ denote the half-space and fault zone layer.
Figure S6. Pre-processing steps for inversion of trapped waves. (a) Velocity seismograms at the JF array generated by event TW2 (see Fig. 15 for location) are corrected for instrument response and rotated to the fault-parallel direction. (b) Bandpass filtering at 2–20 Hz. (c) Integrating velocity to displacement seismograms. (d) Convolving waveforms shown in (c) with $1/t^{1/2}$. Red triangles denote the automatic *S* picks and stations in bold indicate waveforms with clear candidate trapped waves following the *S* arrival.
Figure S7. Inversion results of displacement seismograms at the JF array generated by candidate event TW3. Instead of the simpler model shown in Fig. S5 in the Supporting Information, different shear wave velocities are allowed for the quarter spaces left (QS_SW) and right (QS_NE) to the vertical fault zone layer. (a) Comparison between the observed (black) and synthetic (green) seismograms. (b) Fitness values (green dots) calculated for different FZ parameters tested in the inversion. The parameters

associated with the best-fitting model (black circles) are displayed in each panel and used to produce the synthetic waveforms shown in (a). Parameters named as QS_SW and QS_NE shear velocity represent the values of V_s in the left and right quarter spaces. The best-fitting value for both velocities is 3.1 km s^{-1} suggesting the simpler structure shown in Fig. S5 in the Supporting Information.

Figure S8. Same as Fig. 17 for event TW2.

Please note: Oxford University Press is not responsible for the content or functionality of any supporting materials supplied by the authors. Any queries (other than missing material) should be directed to the corresponding author for the paper.